

Experimental analysis of Taylor bubble regimes using kymography: a tool for understanding bubble ascent dynamics in open-vent volcanic conduits.

Hannah Calleja¹, Eric C.P. Breard^{1,2}, Tom D. Pering^{3,4}, Linda A. Kirstein¹, Ian B. Butler¹, J. Godfrey Fitton¹.

¹ The University of Edinburgh, School of GeoSciences, King's Buildings, Edinburgh, United Kingdom

5 ² Department of Earth Sciences, University of Oregon, Eugene, OR, United States

³ The University of Sheffield, School of Geography and Planning, Winter Street, Sheffield, United Kingdom

⁴ VolcanoTech, The Innovation Centre, 217 Portobello, Sheffield, S1 4DP

Correspondence to: Hannah Calleja (H.Calleja@sms.ed.ac.uk)

Abstract. Taylor bubbles, or gas slugs, are elongated gas pockets that drive discrete and cyclic Strombolian explosions. To understand the surface dynamics of such eruptions, it is essential to first characterize the subsurface flow behaviour within the shallow (<1 km) volcanic plumbing system. This can be achieved experimentally by simulating Taylor bubble flow under
10 conditions that are mathematically scalable to volcanic conduit settings. This paper presents a novel application of kymography – an existing visual analysis technique – for measuring isolated or continuous Taylor bubble flow experimentally in vertical cylindrical pipes. Kymographs condense thousands of frames of experimental footage into a single space-time image, enabling efficient analysis of flow dynamics. The method utilises open-source software (ImageJ), affordable experimental equipment, and straightforward calibration, making it both cost-effective and widely accessible. Here, we illustrate the value of
15 incorporating kymography to simplify and enhance data retrieval from complex two-phase fluid problems which provide a rigorous first order understanding of the flow processes governing surface eruption dynamics exhibited by open-vent basaltic volcanoes. We show that kymography serves as a valuable and effective visual analysis tool for the experimental measurement of gas volume fraction, gas and liquid slug velocities, bubble length and diameter, falling film thickness, bubble and coalescence event counts, and to indicate steady state ascent. In a volcanic conduit, these parameters have important
20 implications for flow stability, interaction dynamics, overpressure development, and the volume of gas released at burst, which ultimately aids our ability to understand and predict eruption style, periodicity, repose, and explosivity level.

Non-technical summary. Some volcanic eruptions are driven by huge gas pockets called Taylor bubbles. Volcanologists use experiments that replicate flow inside volcanic conduits to study these eruptions. We show for the first time that kymography
25 – an open-access tool that condenses thousands of frames of experiment footage into one measurable image – can be used to quantify key Taylor bubble flow parameters to help us understand the frequency and explosivity level of bubble-driven eruptions, and the gaps in between.

30 Notation

Mathematical notation and abbreviations in the order that they appear in the text:

GVF – gas volume fraction.

fps – frames per second.

D – internal diameter of the tube or volcanic conduit, m.

35 FOV – field of view.

μ – liquid viscosity, Pa·s.

ρ – liquid density, $\text{kg}\cdot\text{m}^3$.

σ – interfacial tension N·m.

CV – Coefficient of variation.

40 Fr – Froude number, dimensionless velocity.

Re_b – bubble Reynolds number, dimensionless ratio of inertial to viscous forces.

$E\ddot{o}$ – $E\ddot{o}tv\ddot{o}s$ number, dimensionless ratio of buoyancy to surface tension forces.

Mo – Morton number, dimensionless ratio of viscosity, buoyancy, and gravity forces.

N_f – dimensionless inverse viscosity.

45 ROI – region of interest.

v_b – Taylor bubble ascent velocity, ms^{-1} .

L_b – Taylor bubble length, m.

L_l – length of the inter-bubble space, or liquid slug, m.

LL – Liquid level, m.

50 D_b – Taylor bubble diameter, m.

λ – falling film thickness, m.

LL_L – the liquid level in the tube without bubbles, m.

LL_{+g} – the combined height of liquid and gas in the tube during gas injection, m.

L_g – the height of gas only within the tube during gas injection, m.

55 V_{L+g} – the combined volume of liquid and gas in the tube during gas injection, m^3 .

V_g – the volume in the tube made up of gas only, m^3 .

r – the internal radius of the tube or conduit, m^3 .

VMT – velocity measurement tool.

t_{base} – the point coordinate of one end of the vertical length line ROI that overlaps the band line representing the Taylor bubble

60 base, s.

t_{nose} – the point coordinate of one end of the vertical length line ROI that overlaps the band line representing the Taylor bubble nose, s.

λ' – dimensionless falling film thickness.

1. Background

65 1.1. Bubble-driven volcanic eruptions & other Taylor bubble phenomena

Low viscosity volcanic systems exhibit a variety of eruption styles with variable intensities within short time periods (*Gaudin et al., 2017*). Eruption dynamics are primarily driven by the ascent and burst dynamics of gas from within volcanic conduits. Characterising the fluid dynamics of gas bubbles as they ascend within the conduit – particularly their morphologies, velocities, and interaction behaviours – is critical in improving our understanding of surface
70 explosivity and eruptive style transitions. Since we cannot directly observe the inner workings of a volcano, the mechanisms of bubble formation, interaction, and ascent are inferred using observations of eruptions visible at the surface, samples of erupted material, and laboratory experiments designed to imitate known volcanic conditions. Much of what is known about the flow dynamics inside volcanic conduits comes from an extensive series of experimental studies designed to closely replicate in-conduit behaviours in conditions that are safe, controlled, and quantifiable. In the simplest terms, we can
75 think of a basaltic open-vent volcanic conduit as a kilometres-long cylindrical transport pathway for magma and a separated phase of buoyantly ascending bubbles, where eruptions occur as a result of these bubbles bursting at the free magma surface. Indeed, many models for volcano-scale in-conduit fluid dynamics attribute specific eruptive activity to a series of regimes that are also recognisable in two-phase pipe flow in the engineering literature (*Vergnolle and Jaupart, 1986*). These distinctive bubble morphologies are attributed to specific expressions of surface activity, as shown in Figure 1, of which
80 there are three broad classifications: passive, effusive, and explosive activity. Passive degassing typically involves low gas volume fractions (GVFs) of small spherical or ellipsoid/deformed bubbles emerging from open-vent conduits, lava lakes, or fumaroles. Effusive activity involves the outflow of lava sometimes accompanied by low-level explosive activity, coming from individual or multiple vents. The transition from effusive to explosive activity can occur gradually or rapidly (*James et al., 2008; Maruishi and Toramaru, 2024; Parfitt and Wilson, 1995*), and increasing bubble size significantly increases the
85 possibility that more explosive activity is produced (*James et al., 2009*).

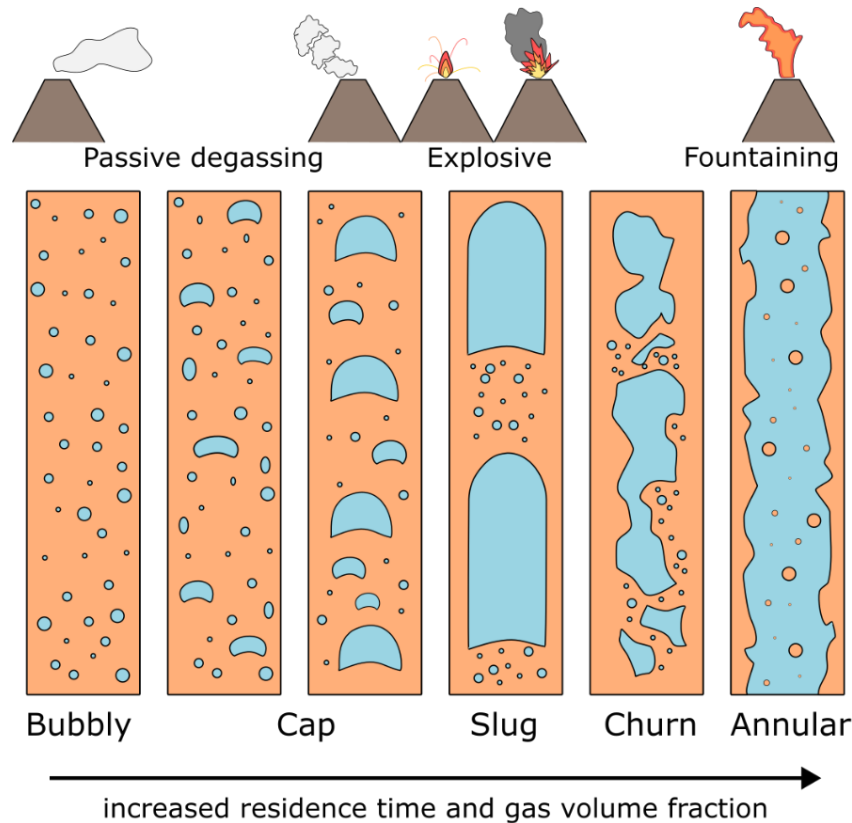


Figure 1: Example flow regimes and the surface eruption styles to which they are attributed. These regimes can be present in tubes at the laboratory scale and in volcanic conduits. Image is adapted from Lehr and Rabbel (2021) and Pering et al. (2017).

90 A key factor in the shift from passive or effusive to explosive behaviour is the formation of Taylor bubbles (also known as
 95 slugs). Taylor bubble formation begins with the exsolution of a limited gas volume from the melt as pressure decreases towards
 the surface (*Gardner et al., 2022; Sparks, 1978*). The exsolved bubbles remain small and compressed until the amount of
 gas and the surrounding pressure reaches a critical value and bubbles decouple from the magma and rise as a separate phase
 (*James et al., 2004*). Small spherical or slightly elongated or deformed bubbles transition into spherical cap and Taylor bubble
 100 morphologies by expansion-driven coalescence (*Parfitt, 2004; Parfitt and Wilson, 1995*), or as a result of the sudden collapse
 of an accumulated foam layer (*Jaupart and Vergnolle, 1989*). The bubble diameters become close to conduit (diameter)-
 filling, with morphologies that can be characterised by the presence of a nose, body and base, or tail, with a surrounding liquid
 falling film and trailing liquid wake (*Llewellyn et al., 2012*). This change in bubble morphology drives a transition in flow
 regime to the extent that their governing fluid dynamics also change, and the conduit diameter (in addition to the pre-existing
 characteristics of the host magma) becomes a major control on bubble ascent. Taylor bubbles are classified as such when their
 length is greater than 1.5 times the surrounding conduit diameter (*Llewellyn et al., 2012; Shosho and Ryan, 2001*), or when the
 surrounding liquid falling film has a length larger than or equal to the surrounding conduit diameter (*Davies and Taylor, 1950*).

The ascent of single Taylor bubbles occurs due to sporadic releases of limited gas volumes into the conduit, and continuous Taylor bubble flow occurs due to moderate rates of continuous gas release (*Seyfried and Freundt, 2000*).

105 Taylor bubbles are most known in volcanology as the drivers of discrete and cyclic VEI 1 - 3 (mild to moderate) Strombolian explosions that are archetypal to Stromboli, but also observed at Etna, Yasur, Pacaya, and Erebus, among others. Strombolian explosions are one of the most widespread expressions of uninterrupted basaltic sub-aerial volcanism globally (*Pering et al., 2016; Pering and McGonigle, 2018*). Experimental studies of two-phase flow in conditions that are scalable to volcanic systems are the key to understanding the in-conduit flow dynamics driving these explosions because they facilitate the measurement of key bubble and liquid flow parameters (e.g., bubble velocity, bubble morphology, falling film thickness, and coalescence processes). These parameters influence the overall stability of the flow, the interaction dynamics between bubbles, the circulation dynamics of magma within the conduit, and the volume of gas released at burst, which ultimately enhances our understanding of the mechanisms for eruption periodicity, repose, explosivity, and the transitions between eruptive styles. Indeed, our current knowledge of the fluid dynamics of Taylor bubbles within volcanic conduits – whether ascending in isolation or within a train – is built upon an extensive foundation of experimental studies (Table 1). Taylor bubbles are a subject of broad interdisciplinary interest in both research and industry (*Morgado et al., 2016*). Outside of volcanology, Taylor bubble flow is relevant to the study of microfluidics and capillary flows (*Etminan et al., 2021*), buoyancy driven fermenters, production and transportation of hydrocarbons in the oil and gas industry (*Ambrose, 2015*), emergency cooling of nuclear reactors, and the boiling and condensing processes in thermal power plants (*Aql and Al-Safran, 2024*). Understanding how Taylor bubbles flow in pipes is important to many fields, and thus their accurate measurement and analysis is essential. By refining our ability to measure and interpret the experimental dynamics of Taylor bubbles under conditions that suitably scale volcanically, we can improve our capacity to anticipate transitions in eruption behaviour.

1.2. Experimental measurement of Taylor bubbles

In volcanology, the key parameters of interest surrounding Taylor bubble ascent are investigated for their role in governing flow-conditions and ultimately surface eruption dynamics. These parameters include gas volume fraction, gas and liquid slug velocities, bubble length and diameter, falling film thickness, bubble frequency, and the tracking of coalescence or break-up events. The most commonly used experimental techniques for the measurement of Taylor bubble parameters both within and outside of volcanology are described in Table 1. A review of these is also available in (*Calleja and Pering, 2023*).

130 **Table 1: Existing techniques for the measurement of experimentally generated Taylor bubble flow with example references for each. Bold references indicate studies that investigate volcanic Taylor bubble flow.**

| Category | Measurement Technique | Description | References |
|----------|-----------------------|-------------|------------|
|----------|-----------------------|-------------|------------|

| | | | |
|---------------------------------|---------------------------------------|---|---|
| Digital Image Processing | Visual observation | Point-to-point (frame-by-frame) measurements from visual observations. | (Calleja and Pering, 2023; Jaupart and Vergnolle, 1988, 1989; Llewellyn et al., 2012; Seyfried and Freundt, 2000) |
| | Pulsed Shadow Technique | Short, intense light pulses create shadowgraphs by illuminating the bubbles from behind, allowing for clear visualization of their contours and dynamics. | (Nogueira et al., 2003, 2006) |
| | High speed camera | Footage captured in excess of 250 fps or exposure less than 1/1000. | (Abdulkadir et al., 2021b; Capponi et al., 2016; Kawaji et al., 1997) |
| | Optical Flow | Footage processed to estimate inter-frame motion for tracking bubble velocity, length, interface dynamics etc. | (Metzker et al., 2025; Bürkle et al., 2025) |
| Electrical | Wire-mesh sensors | Detect changes in electrical conductivity as bubbles pass through a grid of electrodes (wire mesh). | (Abdulkadir et al., 2021a; Roitberg et al., 2016) |
| | Capacitance probes | Measure changes in capacitance caused by the presence of a Taylor bubble (dielectric properties differ from the surrounding liquid). | (Abdulkadir et al., 2011, 2021b) |
| | Resistivity/Conductivity probes | Utilise changes in electrical resistance to track bubble position and size. | (De Bertodano et al., 2006; Wang et al., 2020) |
| Pressure | Pressure transducers | Detect pressure changes as liquid is displaced by bubble ascent and burst. | (Del Bello et al., 2015; James et al., 2004, 2006; Seyfried and Freundt, 2000) |
| Acoustic | Ultrasonic and Infrasonic sensors | Utilise sound waves generated by bubble ascent, interaction and burst to detect bubble movement and size. | (Kobayashi et al., 2010; Lane et al., 2013) |
| Laser-based | Particle Image Velocimetry | Traditionally a laser optical method that provides flow visualisation and velocity measurements by illuminating tracer particles in the fluid. Now also available without lasers. | (Bugg and Saad, 2002; Cerqueira and Paladino, 2020; Nogueira et al., 2006) |
| | Laser Doppler Anemometry/ Velocimetry | Uses laser beams and the Doppler shift of the reflected light to calculate bubble velocity. | (Benattalah et al., 2011; Marić, 1983) |

Magnetic Resonance Imaging

Uses magnetic fields and radio waves to create detailed images of bubbles and surrounding flow patterns. (Kemper et al., 2021)

Non-intrusive optical methods such as high-speed imaging, visual observations, and the pulsed shadow technique are typically used to track bubble ascent velocity and morphology in transparent media (*Calleja and Pering, 2023; Jaupart and Vergnolle, 1988, 1989; Llewellyn et al., 2012; Seyfried and Freundt, 2000*). Traditional laser-based approaches like particle image velocimetry (PIV, now widely available as a digital image processing method without lasers) and laser doppler anemometry (LDA) enable precise velocity field and bubble interface measurements using tracer particles. These techniques are more accessible and offer non-intrusive methods for acquiring data at high spatial resolutions. However, their use is limited to transparent media (*Calleja and Pering, 2023*), and analysis can be computationally intensive at high frame rates. Electrical methods such as wire-mesh sensors and capacitance probes are commonly used to quantify bubble frequency, velocity, and length in opaque systems. These techniques provide real-time data at a low cost, and function well under a wide range of pressure and temperature conditions. However, their reliance on fluid conductivity to function means they are highly sensitive to environmental change and thus require regular recalibration; they are also ineffective in non-conductive fluids and need to be in direct contact with the flow to function. Pressure transducers provide time-resolved measurements of the pressure fluctuations associated with bubble ascent and bursting, while acoustic methods capture bubble dynamics through sound emission; these techniques are useful in optically inaccessible setups. Both methods are sensitive to noise or interference, and have reduced accuracy for bubble size measurements, but are capable of generating high accuracy velocity measurements. They have a wide application range including in extreme environments, and are used in the volcanic literature to experimentally link Taylor bubble ascent velocity and burst dynamics with pulsatory Strombolian eruption dynamics (*Del Bello et al., 2015; Seyfried and Freundt, 2000*). Magnetic resonance imaging (MRI) provides a 3D reconstruction of internal flow structure but is limited in application by its high cost and low temporal resolution.

We present a novel application of kymography – an existing digital image analysis technique – as an approach that is well-suited to measuring experimental Taylor bubble flow parameters such as gas volume fraction, gas and liquid slug velocities, bubble length and diameter, falling film thickness, bubble frequency, and to track coalescence or break-up events.

1.3. Kymographs

Kymographs – also referred to as time-space plots, dynamic motion analysis plots, rise diagrams, motion-track diagrams, or simply as a reslice – are a way to represent dynamic processes as time-space data in a single image. They are often applied to the visualisation of micron-scale dynamic processes in disciplines outside of volcanology wherein parameters such as the direction, speed, fluxes, and growth dynamics of the object/s of interest can be characterised. Examples include tracking the formation, division, growth, and geometry of cellular components (*Mangeol et al., 2016*), characterising velocity fields in microflows (*Le and Fenech, 2022*) and flow characterisation in porous media (*Browne et al., 2020; Haward et al., 2021; Pak*

et al., 2018). In the Earth sciences, traditional kymographs (specifically a revolving paper-wrapped drum on which a stylus recorded motion changes over time) were used in seismography. In contemporary volcanology, kymographs are used to parameterise the frequency, height, and duration of both explosive and effusive eruptions, and to illustrate surface activity transitions over time e.g., for volcanic jets (*Eibl et al., 2023; Muñoz et al., 2022; Spina et al., 2023; Taddeucci et al., 2023; 165 Walter et al., 2023*), gas emissions (*Gaudin, 2017; Vossen et al., 2024*), or ash plumes (*Walter et al., 2020*). Kymographs are also used to capture flow propagation and characterise coherent structures in pyroclastic density currents (*Penlou et al., 2023; Trolese et al., 2024; Uhle et al., 2024*).

In this paper we demonstrate, for the first time, the use of kymography as an effective digital image processing tool for the analysis of experimental Taylor flow in the context of Taylor bubble-driven volcanism. While kymography does not directly 170 measure physical parameters e.g., pressure or acoustic variations, it effectively captures the motion of Taylor bubbles via identifiable flow features that facilitate the measurement of key flow parameters. Against the backdrop of existing techniques (Table 1), kymography offers a low-cost, accurate, and accessible visualisation tool that is complementary to sensor based-methods but can also be utilised as a stand-alone method in its own right.

2. Methods

175 2.1. Experimental setup

The basic setup is a simple and cost-effective gas injection system (*Calleja and Pering, 2023*) consisting of a transparent, vertical, open-ended tube (internal diameter (D): 0.036 m) filled with Newtonian fluids (water-glycerol mixtures, viscosity range: 0.001 – 0.79 Pa·s). The tube is fitted with a voltage-controlled air pump that is capable of varied injection volumes (~0.05 – 0.25 GVF), all of which form Taylor bubble flow regimes under the listed conditions (Table 2). Gas ascent is recorded 180 against a white background with a *SONY RX100-V* compact camera at 25 and 100 frames per second (fps), where the camera field of view (FOV) captures a full view of the entire 1.75 m tube length, or a higher resolution close-up view of a 0.15 m segment, respectively. See Appendix Table 1 for specific camera settings. With the exception of water, our experimental conditions can be mathematically scaled to represent the low-viscosity basaltic systems that are commonly associated with Strombolian-style volcanism using dimensionless parameters (Table 2). The principle of dimensionless scaling lies in the 185 assumption that physical processes are scale invariant as long as they are geometrically, kinematically, and dynamically proportional. While the characterisation of physical phenomena employs equations in which dimensional quantities (e.g., velocity, viscosity etc.) are described by SI units, dimensionless quantities are obtained from ratios of dimensional quantities (i.e., they are unitless). They thus provide a numerical description of flow that is applicable to both laboratory and volcanic scales. The important dimensionless parameters used here are the Reynolds, Re , Eötvös, $E\ddot{o}$, Morton, Mo , Froude, Fr , and 190 dimensionless inverse viscosity, N_f , numbers, and are calculated from a combination of tube, or conduit, liquid, or magma, and characteristic bubble properties (Table 2). The experimental conditions have notably lower $E\ddot{o}$ (around four orders of magnitude) than the volcano-scale estimates due to the large diameter of volcanic conduits and the large density difference

between the ascending large bubbles and the host magma. This disparity is justified because $E\ddot{o}$ and Mo can be combined to determine N_f (Table 2) when the critical values for gravity dominance are exceeded ($E\ddot{o} > 40$, also the minimum required threshold for Taylor bubble formation, and $Mo > 10^{-6}$) (Llewellyn *et al.*, 2012; Seyfried and Freundt, 2000; Viana *et al.*, 2003), thus overlapping N_f values between experimental and volcanic conditions indicates appropriate scaling. Although water does not scale to volcanic conditions, we include it because its prevalence in the literature and well-documented fluid dynamics facilitates data comparison with existing studies. The primary goal of this paper is to evaluate the viability of kymography as a method for Taylor bubble flow analysis rather than discuss specific implication for volcanic activity, thus justifying the use of water despite its scaling limitations in volcanic contexts.

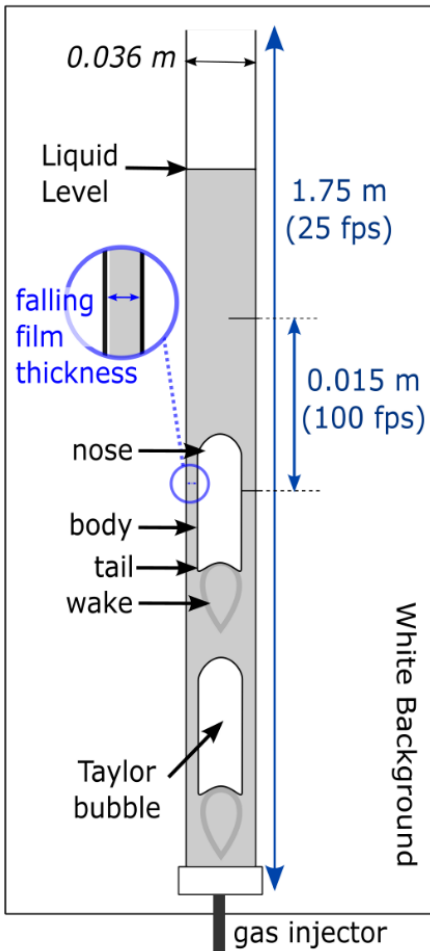


Figure 2: Experimental setup with annotated Taylor bubble components.

205 **Table 2: Dimensional and dimensionless parameters for the explored experimental conditions representing an open-vent basaltic conduit compared with typical Strombolian parameters from Del Bello et al., 2012; James et al., 2004, 2008; Llewellyn et al., 2012; Manta et al., 2019.**

| Symbol (unit) | Lab scale | Volcano Scale |
|------------------------------|-------------------------------|-----------------------------------|
| ID (m) | 0.036 | 1 – 10 |
| GVF | 0.06 – 0.25 | ~0.2 – 0.4 |
| $stdev$ (%) ^{*1} | 0.12 – 2.13 | - |
| $RMSE$ (%) ^{*2} | 2.37 – 6.53 | - |
| μ (Pa·s) | 0.001 – 0.79 | 10 – 10 ⁵ |
| ρ (kg·m ⁻³) | 997 – 1253 | 1300 – 2600 |
| σ (N·m) | 0.06 – 0.07 | 0.4 |
| Mo ^{*3} | 2.6 x 10 ⁻¹¹ – 3.8 | 10 ² – 10 ⁶ |
| $Eö$ ^{*4} | 174 – 249 | 10 ⁵ – 10 ⁶ |
| N_f ^{*5} | 34 - 2 x 10 ⁴ | 2.1 – 1.2 x 10 ⁴ |
| Fr ^{*6} | 0.52 – 0.71 | 0.1 – 0.35 |
| Re_b ^{*7} | 23 – 1.4 x 10 ⁴ | 0.21 - 4200 |

^{*1} Standard deviation – kymograph precision.

^{*2} Root mean squared error – kymograph precision.

^{*3} Mo is the Morton number, $Mo = g\mu^4/\rho\sigma^3$.

^{*4} $Eö$ is the Eötvös number, $Eö = \rho g D^2 / \sigma$ (Llewellyn et al., 2012) where σ is the interfacial tension between the gas and the liquid.

^{*5} N_f is dimensionless inverse viscosity, $N_f = \frac{\rho}{\mu} \sqrt{gD^3} = \left[\frac{Eö^3}{Mo} \right]^{1/4}$ where $g = 0.981$ (gravity constant).

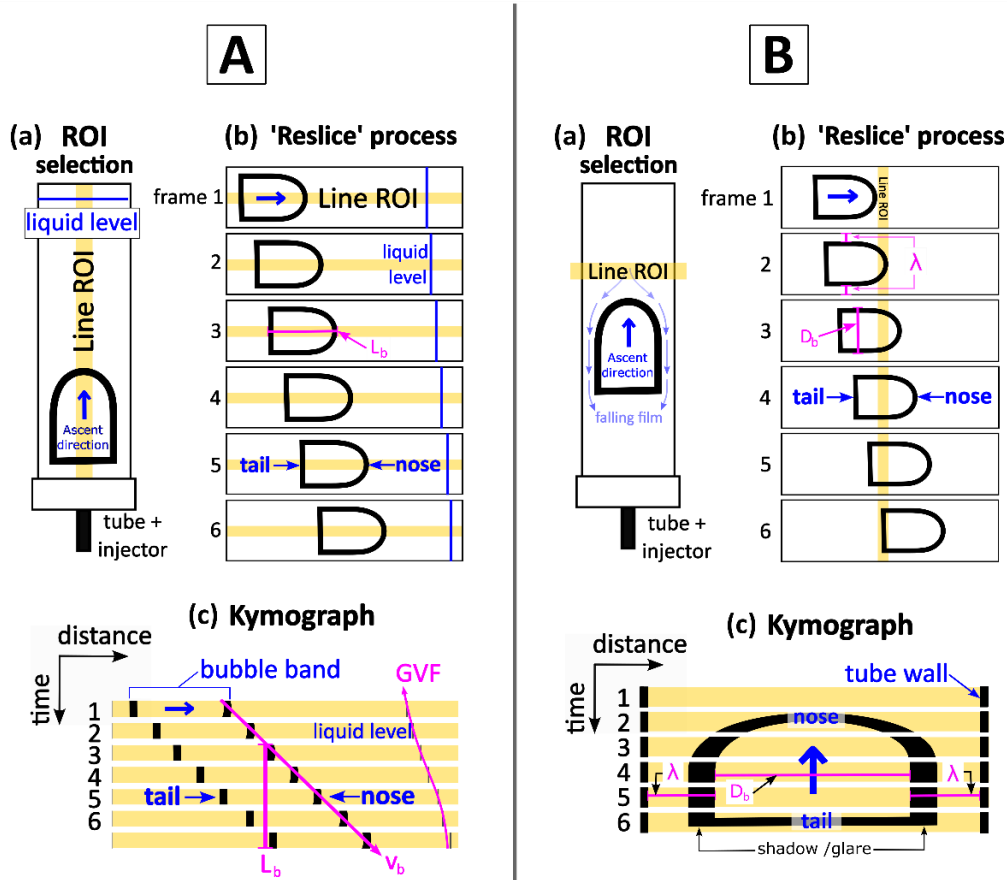
^{*6} Fr is dimensionless velocity, $Fr = v_b / \sqrt{gD}$.

^{*7} Re_b is the bubble Reynolds number, $Re = \rho v_b D / \mu$.

2.2. How to generate and interpret kymographs

210 This method utilises the open-source image processing software ImageJ (Schneider et al., 2012). A kymograph is generated by first loading the relevant experimental footage file into ImageJ in .avi format. Audio information is discarded to conserve storage space. Then, a region of interest (ROI) line is traced on the track along which the target object moves; in this case, this is the Taylor bubble. Figure 2 demonstrates simplified schematics of the kymograph generation process using the example of a single ascending Taylor bubble. The initial line ROI positioning determines which parameters can be extracted from the kymograph. The line ROI should be drawn along the central axis of the bubble and parallel to the path of ascent for Taylor bubble and coalescence counts, Taylor bubble velocity, v_b , Taylor bubble length, L_b , length of the inter-bubble space, L_i , and liquid level, LL . For measurements of Taylor bubble diameter, D_b , and falling film thickness, λ , the line ROI should be drawn so that it is perpendicular to the path of ascent. The kymograph generation process is initiated using the in-built “*image > stacks > reslice*” command in ImageJ’s GUI. An intensity line (a ‘slice’) is generated for each time point, i.e., each frame,

along the line ROI and then plotted along the x-axis. This process repeats so that the intensity lines are stacked vertically along
 220 the y-axis for all frames. The resulting image is a time-space plot (the kymograph), where pixel width corresponds to distance,
 and pixel height corresponds to time. Real (annotated) kymograph samples generated using this method are shown in Figure
 4. Examples of unedited kymographs can be accessed through the links appended at the end of the paper.



225 **Figure 3: Simplified schematics demonstrating the kymograph generation process in imageJ using a single Taylor bubble. First, a**
 line ROI is drawn on the imported footage, either parallel (left image – for measuring bubble velocity and length, and gas volume
 fraction) or perpendicular (right image – for measuring bubble diameter and falling film thickness) to the direction of ascent (a);
 ‘slices’ are taken over the selected line ROI in every frame (b) and then stacked to create a single image with measurable features
 (c) i.e., the kymograph. Key features are shown in blue; the line ROIs required to measure/calculate key flow parameters (Taylor
 bubble and coalescence counts, Taylor bubble velocity, v_b , Taylor bubble length, L_b , length of the inter-bubble space, L_b , and liquid
 230 level, LL, Taylor bubble diameter, D_b , and falling film thickness, λ) on the raw footage compared to the kymographs are shown in
 pink.

Taylor bubble noses and tails appear on the kymographs as lines with high image contrast in the x-direction. The space in
 between these lines (the low-contrast region) represents the body of the Taylor bubble. We refer to these features as they appear
 235 on the kymograph as bubble bands. The spaces in between the bubble bands i.e., between the lines representing the base of a
 leading bubble and the nose of the next bubble ascending in the train, are the inter-bubble spaces, or liquid slugs. We refer to

these features as they appear on the kymograph as liquid bands. Bubble bands are differentiated from liquid bands by the flow direction of the small (<1 cm) entrained bubbles and how they appear on the kymograph as a result of the way they interact with the reslice line ROI (Figure 4A(i)). They can also be identified by the merging of two bubble bands, which indicates a coalescence event (Figure 4A(i)). The number of bubble bands present on the kymograph indicates the number of ascending Taylor bubbles present in the footage sample. Bubble and coalescence event counts can be extracted by simply counting these bands.

The kymographs generated from close-up footage (Figure 4A(i) and B) capture a limited (~ 15 cm) segment of the tube, provide high resolution (captured in 1920×1080 pixels at 100 fps, 60 Mbps) data and are well-suited for measurements of Taylor bubble velocity, length, and diameter, liquid slug length, and falling film thickness (depending on the orientation of the selection ROI). In this case the target segment captures bubbles that have reached steady state, with the exception of low viscosity mixtures with localised turbulence. The full-view kymographs (Figure 4A(ii)) capture all bubble and liquid behaviour (for the parallel selection ROI) from injection to burst: Taylor bubble velocity and length, liquid slug length, liquid level (needed for the calculation of GVF), and all coalescence events. Full-view kymographs can be divided into three regions: the injection instability region, the steady state region, and the burst instability region. The injection instability region begins at the initial injection point and ends at the approximate location along the tube where bubbles tend to enter steady state, and the steady state region begins. The start of the steady state region corresponds to the distance along the tube where Taylor bubbles are observed to stabilise, equivalent to $\sim 16D$ (Taitel *et al.*, 1980), around 0.57 m along the tube. The majority of recorded coalescence occurs in the injection instability region immediately after injection. Bubble bands in this region are labelled as sub-divisions of the bubble they coalesce into upon reaching the steady state region (e.g., B6a – c in Figure 4A(ii)). The burst instability region describes the approximate distance along the tube where the bubbles destabilise before burst.

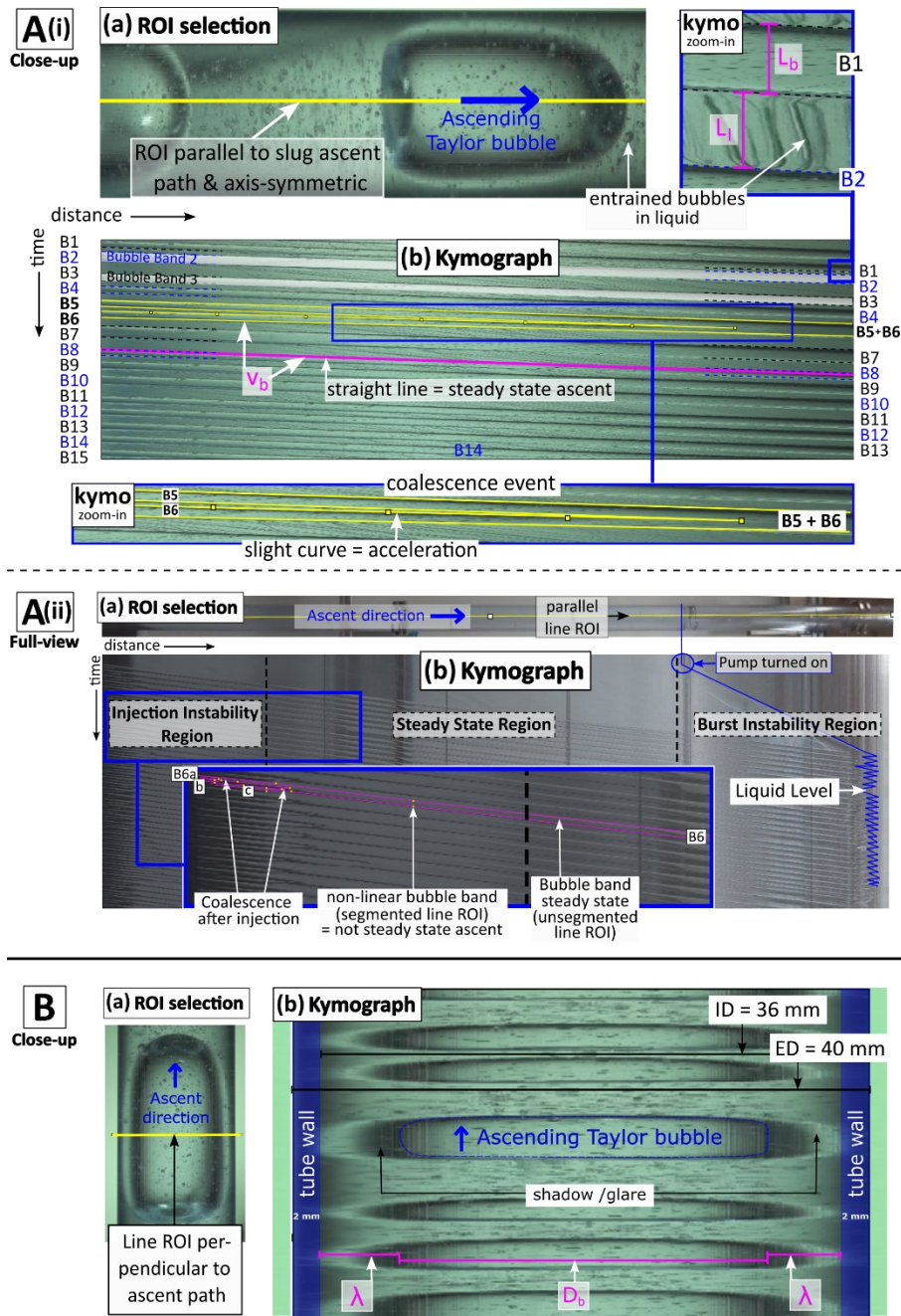


Figure 4: Annotated images of ROI selection and kymographs generated using the methods described in-text; these are labelled A or B to correspond the simplified schematics in Figure 3; the kymographs are generated from selection ROIs parallel (A) or perpendicular (B) to the direction of bubble ascent. Key features are shown in blue; the line ROIs required to measure/calculate key flow parameters (Ai and Aii: Taylor bubble and coalescence counts, Taylor bubble velocity, v_b , Taylor bubble length, L_b , length of the inter-bubble space, L_l , and liquid level, LL; B: Taylor bubble diameter, D_b , and falling film thickness, λ) are shown in pink. A(i) and B are kymographs generated from close-up (100 fps) footage of a centrally located tube segment where-in the Taylor bubbles ascend in steady state. A(ii) is generated from full-view (25 fps) footage that captures the full length of the tube. All the kymographs capture vertical and continuous Taylor flow (GVF = 0.25) in a liquid of 0.95 glycerol fraction.

2.3. Calibration, limitations, error and corrections

Detailed information on camera calibration, distortion correction, pixel-to-meter calibration, error calculation, and filtering and thresholding processes is provided in the Appendices. Pixel to world unit (ms^{-1} , m) calibrations are performed using objects in the image with a known distance e.g., the tube diameter, to determine a scale factor that is later applied to the relevant data.

270 The clarity and readability of the generated kymographs and the data that can be extracted from them are dependent on the frame rate and resolution of the recorded footage, the FOV of the camera, the setup and lighting, and the stability of the recorded flow. Footage showing stable flow produces more coherent kymographs and thus reduced error relative to data from lower viscosity media, even at low framerates. In turbulent flows, such as in water, the larger dispersed bubbles present in the surrounding liquid and the more chaotic flow behaviour generate noisier kymographs and increased precision error. This
275 behaviour is demonstrated in the trends observed in all the measured parameters in water as shown in sections 2.4 – 2.6; the glycerol data demonstrate strong precision between methods and less variation within the same experimental conditions because the overall flow stability is much greater than in water. Measurement precision decreases with increasing kymograph resolution because selection variability increases when pixel coverage is higher, as reflected in the data plots herein.

The precision of pixel selection by the user ('human error') and the distortion caused by the camera lens are combined to give
280 the root-mean-square error (RMSE). Human error was quantified as the standard deviation of repeat measurements of a single feature in millimetres (converted from pixels) for each generated kymograph i.e., based on experiment condition, camera FOV, and the initial ROI selection (parallel or perpendicular to the direction of bubble ascent). The camera has in-camera automatic distortion correction (as determined by performing checkerboard calibration) with calculated mean reprojection errors of 0.91 and 0.14 pixels, equivalent to 0.013 and 0.79 mm, for the close-up and full-view footage FOVs, respectively. Refraction at the
285 curved boundaries along the tube cross section is found to affect all measurements taken perpendicular to the direction of bubble ascent, i.e., bubble diameter and falling film thickness measurements. A correction can be applied to the data retroactively to account for this (see Appendix 4), or it can be corrected for during ROI selection as described in section 2.6. Distortion along the tube length is negligible and primarily driven by the lens distortion in the camera; it is thus accounted for in the calculated error.

290 Image filtering and thresholding techniques including Gaussian, median, and Fourier-transform filters were applied in an attempt to enhance kymograph accuracy but ultimately failed, as they eroded critical features and reduced measurement precision. Automation attempts were also unsuccessful for similar reasons (see Appendix 5). As kymography is further refined, particularly through advances in imaging and AI, its utility for the automated collection of Taylor flow parameters is likely to expand.

295

2.4. Velocity

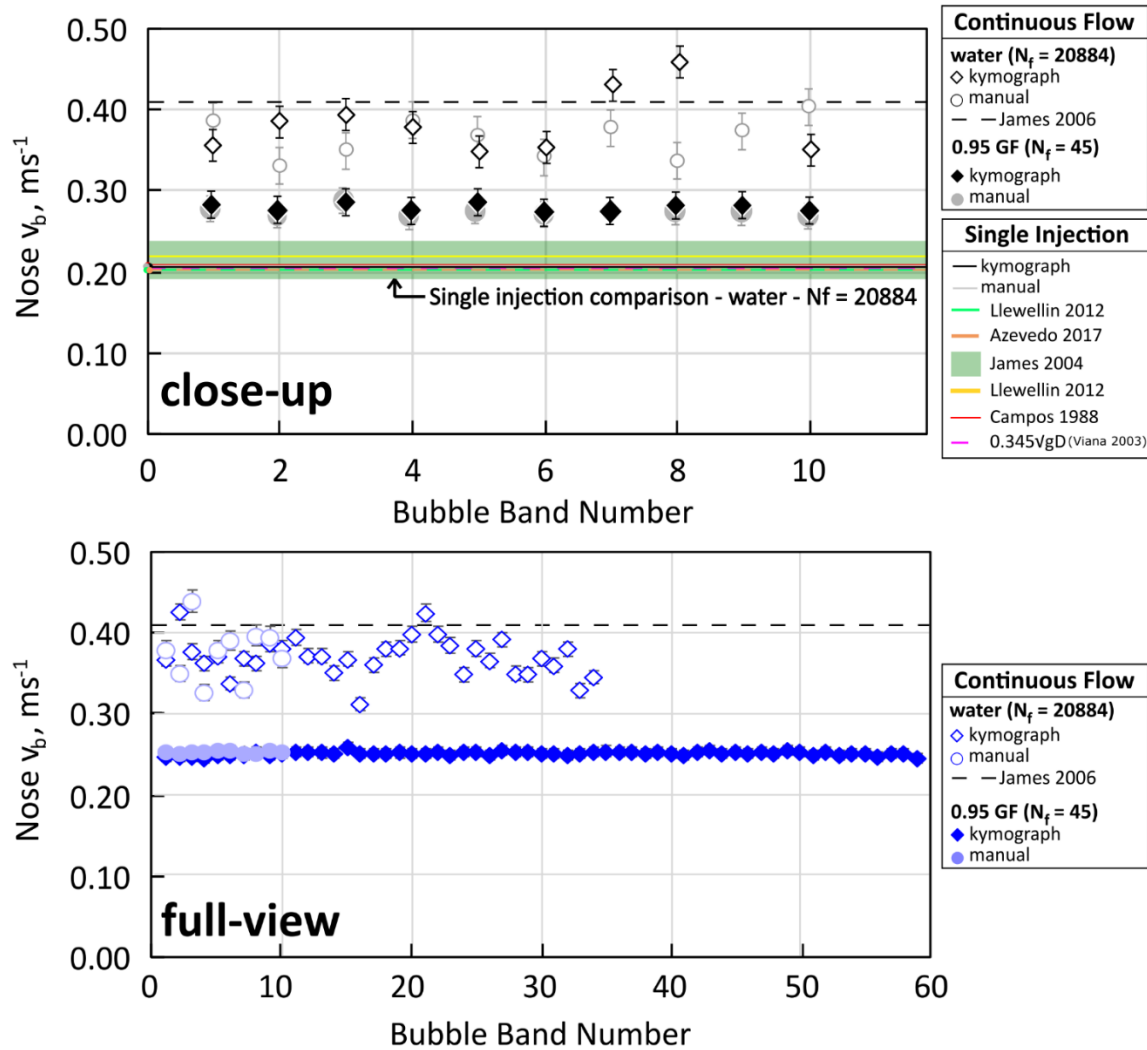
The ascent velocity of volcanic Taylor bubbles (along with conduit geometry and magma viscosity) is a key control on flow stability and overpressure, and thus surface explosivity. Bubble coalescence influences eruption periodicity and repose, and is similarly modulated by magma viscosity and conduit conditions, in addition to bubble and liquid velocities. The ability to observe and measure these parameters experimentally is essential for understanding the in-conduit flow processes that drive surface explosivity and activity transitions. On a kymograph, objects moving with constant velocity appear as straight lines, where the slope of the line is directly proportional to the velocity of the moving object. The velocity of Taylor bubbles rising in steady state is determined by drawing an unsegmented line ROI along the edge of the relevant bubble band on the kymograph, then utilising the “Velocity Measurement Tool” (VMT) macro for imageJ ([https://dev.mri.cnrs.fr/projects/imagej-](https://dev.mri.cnrs.fr/projects/imagej-macros/wiki/Velocity_Measurement_Tool)
305 [macros/wiki/Velocity_Measurement_Tool](https://dev.mri.cnrs.fr/projects/imagej-macros/wiki/Velocity_Measurement_Tool)) to measure the velocity of the line segment in pixels, and scaling to the appropriate unit ($\text{m}\cdot\text{s}^{-1}$) using calibrated measurements. Taylor bubbles ascending in non-steady state appear on the kymographs as non-linear bands, such as during coalescence (Figure 4A(i)) or in turbulent flow. The oscillating movement of Taylor bubbles ascending in a turbulent regime appear as irregular bubble bands which expand and contract in the y-direction on the kymograph. The acceleration of the trailing bubble is illustrated on the kymograph as a slight curvature in the corresponding
310 bubble band as it is captured into the leading bubble wake, up to the point of coalescence. This can also be measured using the VMT with a segmented line instead, so that velocity values are calculated for each line segment.

Figure 5 presents Taylor bubble velocity data from 5 - 30 seconds of experiment footage where Taylor bubbles ascend in steady state in water or a solution with 0.95 glycerol fraction in continuous flow ($\text{GVF} = 0.25$). Results compare well to a sample of 10 point-to-point measurements from the raw footage i.e., where average velocity is calculated from the time taken
315 for the Taylor bubbles to cover a known distance, and data from existing literature. We refer to the point-to-point measurements as ‘manual measurements’ herein. The kymograph data show good agreement to the manual measurements in all cases, especially where flow conditions are more stable. Data from existing literature for similar experimental conditions under continuous flow are scarce, though there is good agreement with data from (*James et al., 2006*). There are, however, many publications exploring a broad range of isolated Taylor bubble ascent parameters (*see Calleja and Pering, 2023; Morgado et al., 2016* reviews and references therein) to which we compare our results. Manual and kymograph measurements were
320 performed for isolated Taylor bubble injections only for comparison to studies where $D = 0.036 \text{ m} \pm 5 \text{ mm}$ and in water. The processed data from the kymographs show good agreement with the studies, within a margin of $0.03 \text{ m}\cdot\text{s}^{-1}$ or 12%. We also compare our results to the theoretical prediction of the ascent velocity of volcanic slugs, v_{sl} , assuming isolated Taylor bubble ascent within a stagnant Newtonian fluid in a vertical tube:

$$325 \quad v_{sl} = 0.345\sqrt{gD} \quad (1)$$

where g is the gravitational constant and D is the internal tube diameter (*Viana et al., 2003*). Measurements in water show greater variation both within the same dataset and between the different methods because of the natural instabilities and turbulence that occurs in this media. Data from stable ascent conditions i.e., the higher-viscosity glycerol data show very little

330 variation between the kymograph and manual measurements. This highlights the efficacy of kymography in this use case, especially in efficiently processing large bubble samples.



335 **Figure 5: Kymograph ascent velocity data compared to results from manual measurements for continuous Taylor flow and a single isolated Taylor bubble injection in identical conditions for close-up and full-view FOVs. The close-up FOV plot compares kymograph measurements from ~ 5 seconds of footage to manual measurements and data from the literature (de Azevedo et al., 2017; Campos and Guedes De Carvalho, 1988; James et al., 2004, 2006; Llewelin et al., 2012) under similar experimental conditions ($0.035 \text{ m} < D < 0.04 \text{ m}$) in water and to the theoretical prediction from Viana et al., 2003. Note that many of these overlap on the plot. The full-view FOV plot shows measurements for ~10-30 seconds of footage under the same conditions. The full-view FOV demonstrates data from ~30 seconds of footage. Calculated error is shown for the kymograph and manual measurements. Error bars that are smaller than the data markers are not visible on the plot.**

340

2.5. Length

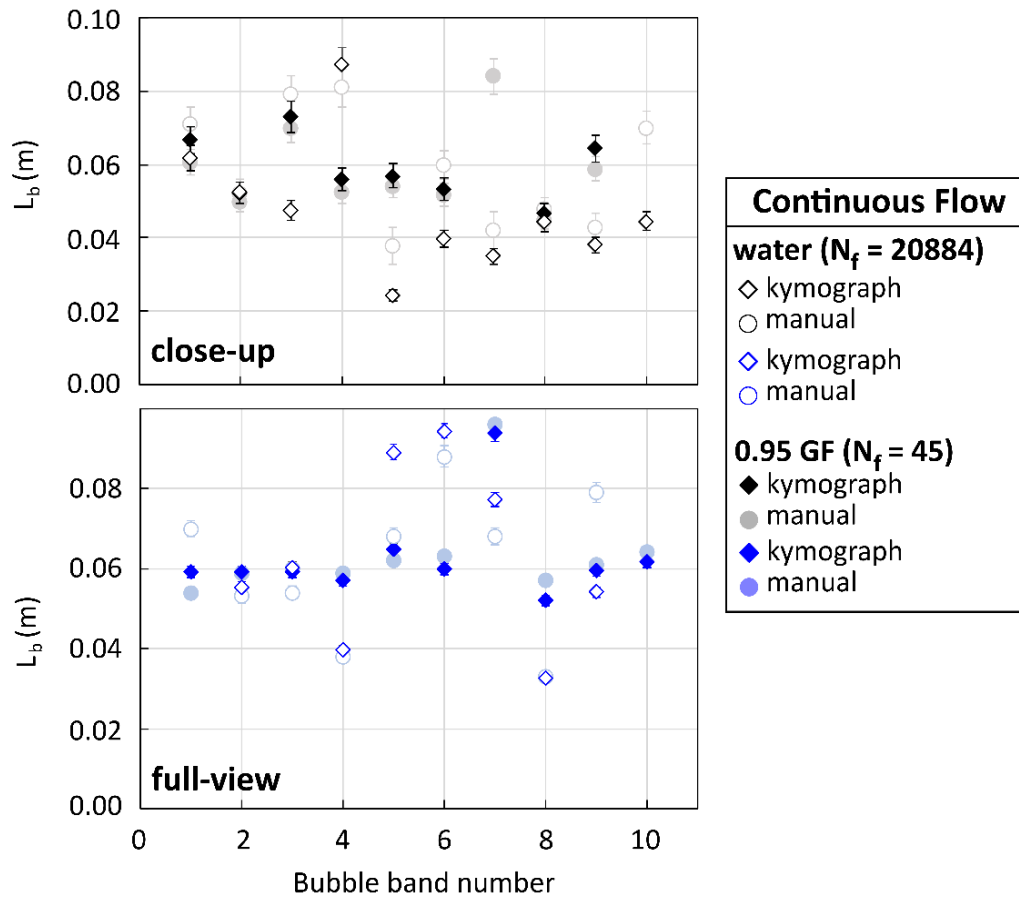
Taylor bubble length influences the volume of gas released at burst, and longer Taylor bubbles are linked to increased overpressure and stronger eruptions at burst (*Del Bello et al., 2012; Suckale et al., 2010*). Understanding the in-conduit controls on Taylor bubble length during ascent via flow experiments improves our understanding of in-conduit gas-liquid dynamics and eruption behaviour at true scale. On a kymograph, the height of the bubble bands and the liquid bands correspond to the length of the Taylor bubbles and the inter-bubble spaces (or liquid slugs), respectively. Taylor bubble length is calculated by first drawing a vertical line ROI which starts at the band line that corresponds to the bubble nose, and ends on the band line that corresponds to the bubble base (Figure 4A(i)) and extracting its time coordinates, then multiplying the converted y-coordinates in seconds by the known ascent velocity as follows:

$$L_b = v_b(t_{base} - t_{nose}) \quad (2)$$

where t_{base} and t_{nose} are the time coordinates, in seconds, which correspond to each point of the vertical line ROI. The length of the inter-bubble space is calculated using an almost identical method where the vertical line ROI is instead positioned to cover the liquid band and the following equation is used:

$$L_b = v_b(t_{nose} - t_{base}) \quad (3)$$

where v_b now refers to the nose ascent velocity of the bubble rising below the inter-bubble space within the train. Figure 6 shows Taylor bubble length data for a sample of 10 bubbles ascending in steady state in continuous flow ($GVF = 0.25$) compared to manual measurements in identical conditions. Taylor bubble length varies in all cases due to both the liquid properties and the coalescence rates, as expected for continuous flow. The greatest difference between the manual and kymograph measurements occurs in water because the low-viscosity-driven instabilities in the flow generate lower resolution kymographs and thus increased precision error, as discussed in section 2.3. The manual and kymograph measurements are shown to agree well where flow conditions are stable.



365 **Figure 6: Kymograph Taylor bubble length data compared to results from manual measurements for continuous Taylor flow. Kymograph data are missing from bubble band numbers 7 and 10 on the close-up plot because the velocity data required to calculate length was unavailable due to coalescence, or because the end of the sample was reached, respectively.**

2.6. Falling film thickness and bubble diameter

The falling film refers to the thin layer of liquid flowing downwards along the boundary between the Taylor bubble and the tube walls (*Llewellyn et al., 2012*). The thickness of the falling film has implications for bubble stability, shape, velocity, wake
 370 behaviour and coalescence dynamics. In a volcanic conduit, the thickness of the falling magma film surrounding Taylor bubbles influences the development of overpressure and thus eruption explosivity (*Del Bello et al., 2012*). To measure bubble diameter and falling film thickness, the kymograph must be generated from the close-up FOV footage and using a line ROI that is perpendicular to the bubble ascent path. The resulting kymograph provides a stretched view of the target bubbles and the features needed for measurement (Figure 4B). Differentiation of the bubble boundaries from the regions of shadow or
 375 contrast caused by the refraction of light through the tube and the liquid is crucial for accurate measurements. Misidentification

of the bubble boundaries leads to underestimating falling film thickness, and overestimating bubble diameter beyond the known internal diameter of the tube. By using the known tube dimensions, it is possible to accurately identify the bubble boundaries. Once these features are correctly identified, bubble diameter and falling film thickness are measured using horizontal line ROIs as shown previously in Figure 4B, then converting to the appropriate unit. This method of ROI selection
380 negates the need to mathematically correct the data for the effects of refraction at the curved boundaries along the tube cross-section, as evidenced by agreement with experimental and theoretical data from the literature. An alternative approach for measuring bubble diameter and falling film thickness which requires post-processing corrections to account for image distortion by diffraction is available in Appendix 4.

There are several empirical correlations in the literature that estimate dimensionless film thickness, λ' , as a function of Re or
385 N_f , that are valid for isolated Taylor bubble ascent under our experimental conditions (*de Azevedo et al., 2017; Karapantsios and Karabelast, 1995; Lel et al., 2005; Llewellyn et al., 2012*). The theoretical λ' for each correlation was calculated and then used to determine predicted λ :

$$\lambda = \lambda' r \quad (4)$$

as rearranged from Llewellyn et al. (2012). Under the assumption of an axis-symmetric laminar falling film, the predicted film
390 thickness can be used to calculate theoretical bubble diameter for the same experimental conditions:

$$D_b = D - 2\lambda \quad (5)$$

The plots in Figure 7 demonstrate good agreement between the kymograph and manual measurements of diameter and falling film thickness, and also between the kymograph measurements with the available theoretical and experimental data for the diameter and falling film thickness of isolated Taylor bubble ascent. Where flow is stable, the single injection predictions agree
395 well with the kymograph data for continuous Taylor flow. This is not always the case for unstable flow, where film thickness is underpredicted by the literature correlations compared to both manual and kymograph single injection measurements.

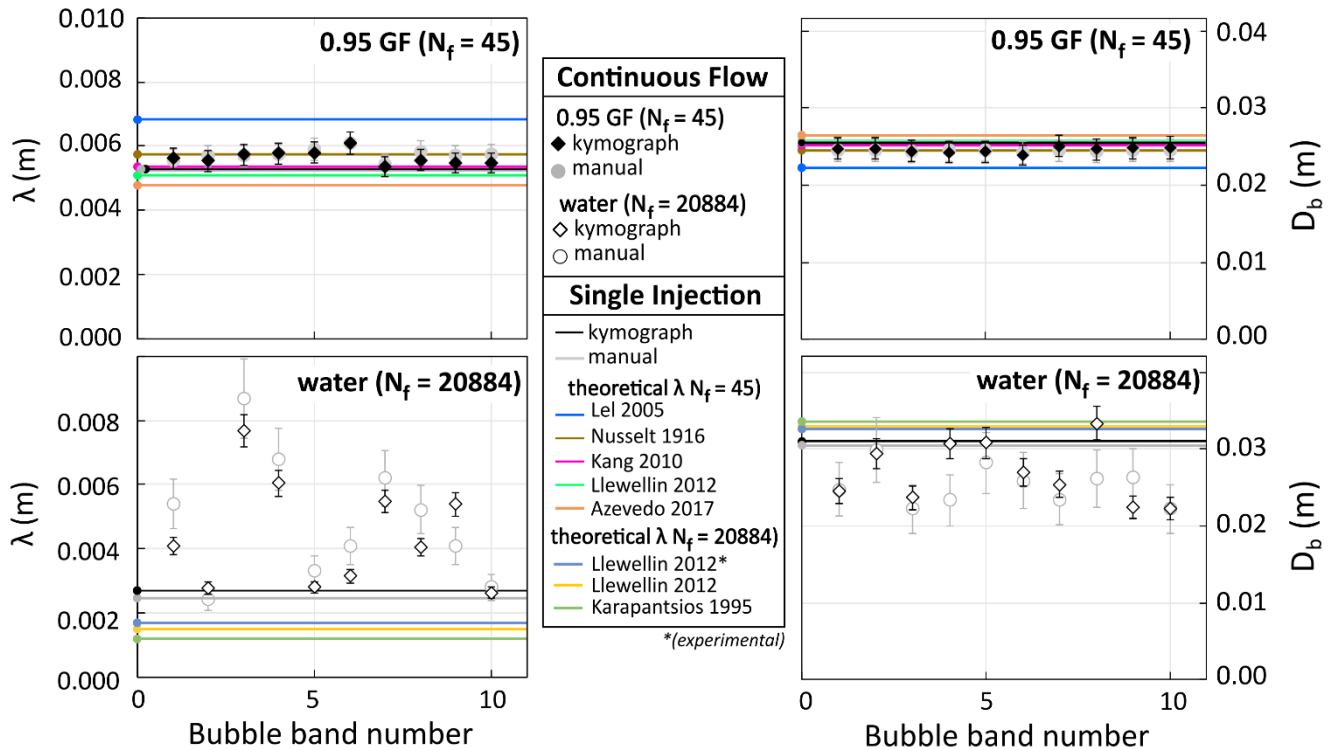


Figure 7: Taylor bubble diameter and falling film thickness. Kymograph data is compared to results from manual measurements for continuous Taylor flow in identical conditions. Single injection kymograph and manual data are also compared to estimates from empirical correlations in the literature (de Azevedo et al., 2017; Kang et al., 2010; Karapantsios and Karabelast, 1995; Lel et al., 2005; Llewellyn et al., 2012; Nusselt, 1916). Calculated error is shown for the kymograph and manual measurements.

2.7. Gas volume fraction

In gas-rich basaltic systems, the gas volume fraction (GVF) within the conduit plays a fundamental role in modulating the style, periodicity, and intensity of eruptive activity. GVF serves as both a diagnostic parameter for in-conduit flow conditions and a first-order control on explosivity and surface eruption dynamics. The critical GVF required for stable slug formation and ascent defines the onset conditions for Strombolian activity, where the coupling between the Taylor bubble and the overlying magma determines whether sufficient overpressure can accumulate to generate an explosion at the surface. As such, it is vital that we are able to determine the GVF within the experimental system to ensure volcanic scalability (Table 2).

Liquid level fluctuations can be quantified on a kymograph to calculate the GVF within an experimental system, and to determine the full gas injection capability of a pump (Figure 8). To measure liquid level fluctuations throughout an experiment run, the line ROI used to generate the kymograph must pass through the end of the tube. Once generated, the tube end appears on the kymograph as a vertical line. Numerous measurement ROIs can then be drawn to span the distance between the liquid level line and line representing the top of the tube. GVF is calculated by extracting the time coordinates and line length in pixels, performing appropriate unit conversions, and then inputting the values into the following equations:

415

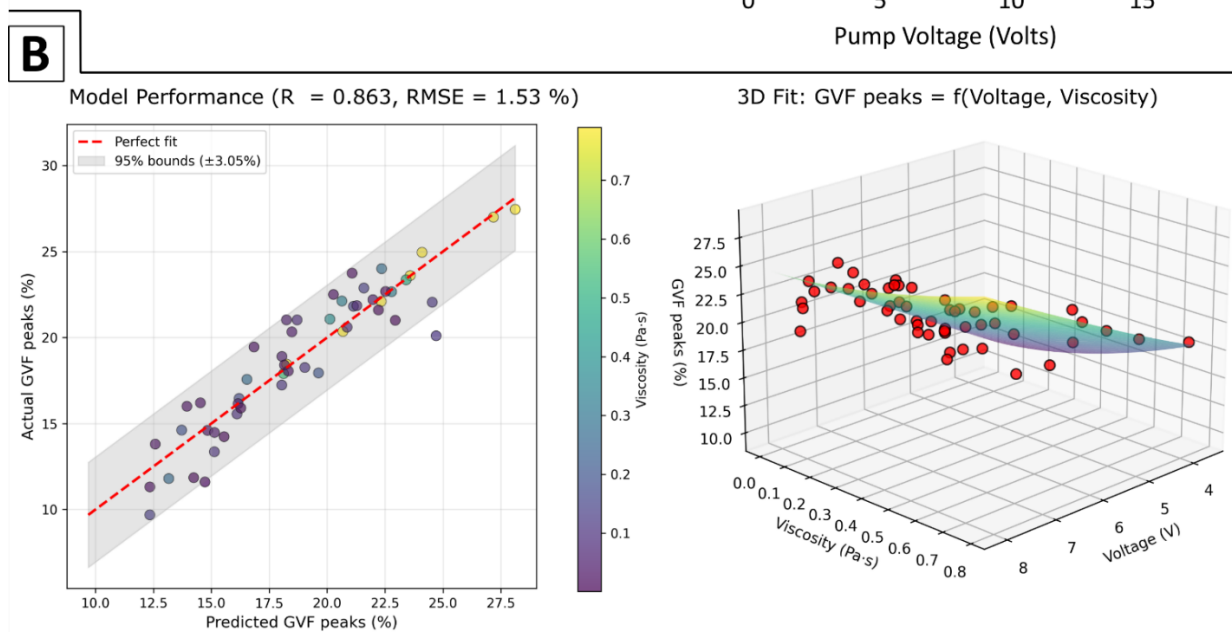
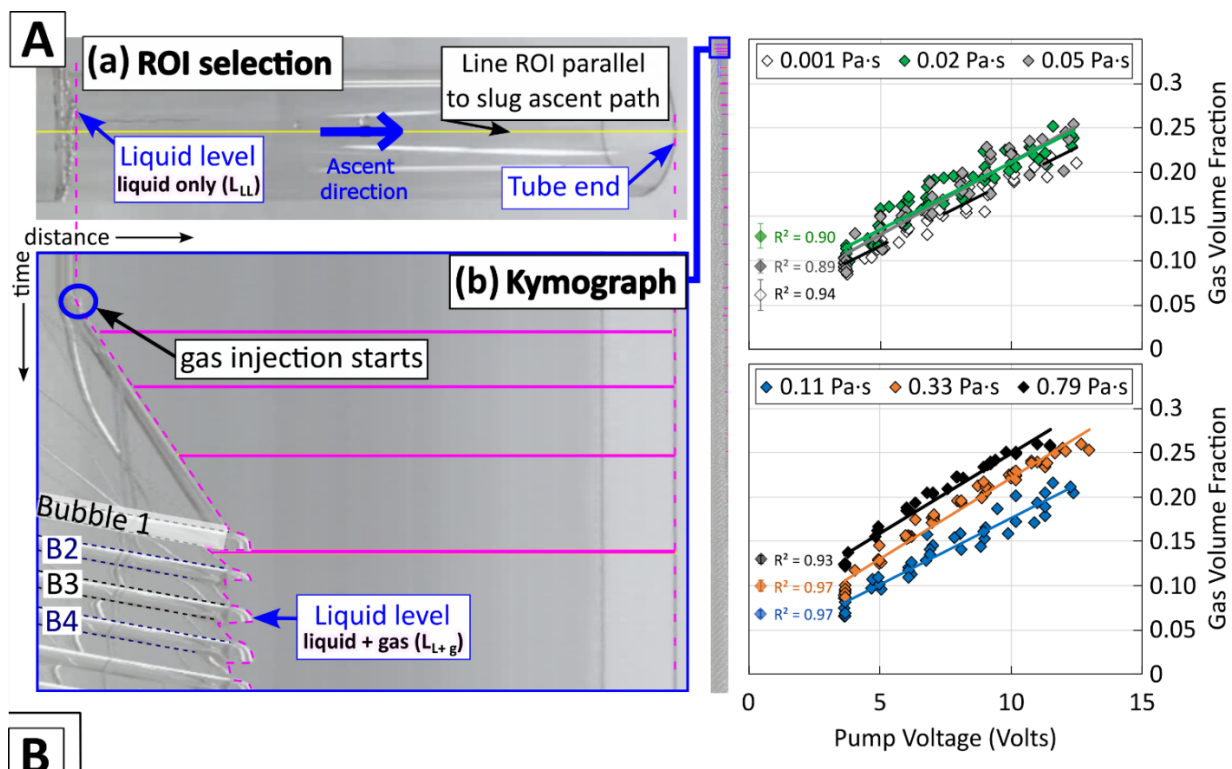
$$L_g = L_{L+g} - L_{LL} \quad (6)$$

$$V_{L+g} = \pi r^2 L_{L+g} \quad (7)$$

$$V_g = \pi r^2 L_g \quad (8)$$

$$GVF = \left(\frac{V_g}{V_{L+g}} \right) \quad (9)$$

where L_{LL} is the length of the liquid level in the tube without bubbles, i.e., before the pump is active, L_{L+g} is the fluctuating liquid level in the tube in meters during gas injection, L_g is the length in the tube in meters that is made up of gas only, V_{L+g} is the volume of liquid and gas in the tube during the gas injection process in meters cubed, V_g is the volume of gas only in meters cubed, and r is the internal radius of the tube in meters. We demonstrate the use of this method to determine the injection capability of a Delaman® 12 Volt DC miniature diaphragm pump for a range of liquid viscosities in Figure 8A, then show how these data be can used to develop a model that predicts GVF within an experimental system where pump voltage and liquid viscosity are known Figure 8B. Gas volume fraction is shown to increase with increasing pump input voltage as expected. The model predicts GVF peaks with an R^2 of 0.863 and a root mean square error of 1.5%; individual predictions have uncertainty of approximately $\pm 3.1\%$ at the 95% confidence level. Full details are available in Appendix 6.



430 **Figure 8: Liquid level and gas volume fraction (GVF).** [A] shows close-up view of the ROI selection (a) and (b) a small segment
 435 (annotated) of the entire kymograph generated to demonstrate measurements of liquid level fluctuations as pump input voltage is
 varied; these are used to calculate the gas volume fraction within the experimental system. The kymograph captures vertical and
 continuous Taylor flow (~4–12 Volts or GVF = 0.05 - 0.25) in a liquid of 0.95 glycerol fraction. The plots show the full GVF capability
 range of the pump (note the line for the 0.02 Pa·s fluid overlaps the line for the 0.05 Pa·s fluid and that error bars for each dataset
 are displayed next to the corresponding r-squared value). [B] demonstrates the model performance (left) and 3D fit based on the
 model equation: $GVF_{peaks} = 16.465 \cdot V^{-0.491} \cdot \mu^{1.668} + 2.789 \cdot V + 1.884$.

3. Concluding remarks

Taylor bubbles are recognized in volcanology as key drivers of Strombolian explosions, a prevalent form of basaltic sub-aerial volcanism. The accurate measurement and analysis of their flow parameters experimentally is essential to our understanding of subsurface Taylor bubble ascent dynamics at volcanic scales, and thus the potential to predict changing surface eruptive activity. This study demonstrates, for the first time, the application of kymography as a tool for measuring Taylor bubble flow parameters in transparent cylindrical pipes in the context of deepening our understanding of bubble-driven volcanic eruption mechanisms. Key flow parameters can be characterised, including bubble and coalescence event counts, bubble rise velocity, bubble length, liquid length, bubble diameter, falling film thickness, and gas volume fraction. In a volcanic conduit, these parameters have important implications for flow stability, interaction dynamics, overpressure development, and the volume of gas released at burst, which ultimately aids our ability to understand and predict volcanic eruption style, periodicity, repose, and explosivity level. In transparent cylindrical tubes, we show kymography to provide precise measurements even under turbulent flow conditions and at low resolutions (25 fps). Measurement precision is influenced by factors such as frame rate, camera field of view, lighting, flow stability, and the rectilinearity of the lens used for image acquisition. The accuracy of this method, validated through agreement with experimental and theoretical data from similar studies (*de Azevedo et al., 2017; Campos and Guedes De Carvalho, 1988; James et al., 2004, 2006; Kang et al., 2010; Karapantsios and Karabelast, 1995; Llewellyn et al., 2012; Nusselt, 1916; Viana et al., 2003*), establishes kymography as a simple and effective tool for capturing detailed Taylor-bubble flow data experimentally. This method utilises an accessible and cost-effective experimental setup and open-source software, and is well-suited for the investigation of bubbles ascending with axisymmetric ascent paths in transparent media. In the context of Taylor bubble-driven volcanism, kymography is a powerful open-access tool that can facilitate efficient interpretation of analogue experiments that vitally provide a rigorous first order understanding of the governing flow processes in volcanic conduits.

Appendix 1. Camera information

460 Appendix Table 1: Camera model and shoot settings.

| | |
|-------------------------------------|---|
| Make and Model | <i>SONY RX100-V</i> |
| Shoot mode | <i>Movie</i> |
| Recording format | <i>XAVC S HD (1920 x 1080 pixels)</i> |
| Record settings | <i>100 fps 60 Mbps or 25 fps 60 Mbps</i> |
| Focal length | <i>24 mm (pre-set)</i> |
| Raw file format | <i>.MP4</i> |
| Storage file path | <i>PRIVATE > MPROOT > CLIP or MPROOT > 100ANV1</i> |
| Distance from tube to camera | <i>Close-up FOV: 0.3 m Full-view FOV: ~2 m</i> |

Appendix 2. Distortion by the camera lens

Camera calibration was performed prior to all experiments to assess the need for distortion correction and to evaluate the in-built correction capabilities of the cameras. Each camera view (close-up and full-view) was calibrated separately using a checkerboard (rectangular with a clear white border and fixed to a rigid surface) pattern covering $\geq 20\%$ of the field of view (FOV), with different checkerboard sizes selected to suit each view. The calibration workflow followed standard practices (Heikkilä & Silvén, 1997; Zhang, 2008): the camera was fixed on a tripod and manually focused on the tube, and the checkerboard was moved through the FOV at varied angles and orientations to maximise lens distortion coverage, particularly near image edges. Between 10–20 images were extracted from each set of recordings (182 and 400 frames for the close-up and full-view FOVs, respectively) and imported into the MATLAB Single Camera Calibrator App (465 https://uk.mathworks.com/help/vision/ug/using-the-single-camera-calibrator-app.html#responsive_offcanvas). This tool estimates intrinsic and extrinsic parameters via checkerboard corner detection and reports calibration quality through reprojection error, with < 1 pixel generally considered acceptable. Images with high errors were excluded to ensure geometric consistency across the dataset, and calibration accuracy was validated by assessing undistorted image previews. Both camera FOVs yielded mean reprojection errors < 1 pixel, indicating negligible distortion (Zhang, 2008) and confirming that retrospective correction was unnecessary. However, these error values were incorporated into subsequent uncertainty analyses for kymograph-derived measurements. (475

Appendix 3. Error

We use the term ‘human error’ in this context to specifically refer to the variance between measurements from small discrepancies in pixel selection by the user that occur during measurement ROI selections. This was quantified for each kymograph i.e., per liquid viscosity, FOV, and initial ROI selection, by repeatedly measuring a sample of the same features on each kymograph for a total of 180 measurements then calculating the standard deviation of each measurement set (in m or mm as relevant). This is combined with the relevant camera distortion error (depending on the camera settings and FOV; in mm) using the root mean squares error (RMSE) method to give the error bars that are applied to all the data presented in the main text. RSME was calculated using the standard equation:

$$RMSE = \sqrt{\frac{1}{n} \sum_{i=1}^n e_i^2} \quad (1)$$

where:

e_i represents the individual error values, including distortion and precision error, expressed as percentages,

n is the number of error values considered (in this case, $n = 2$),

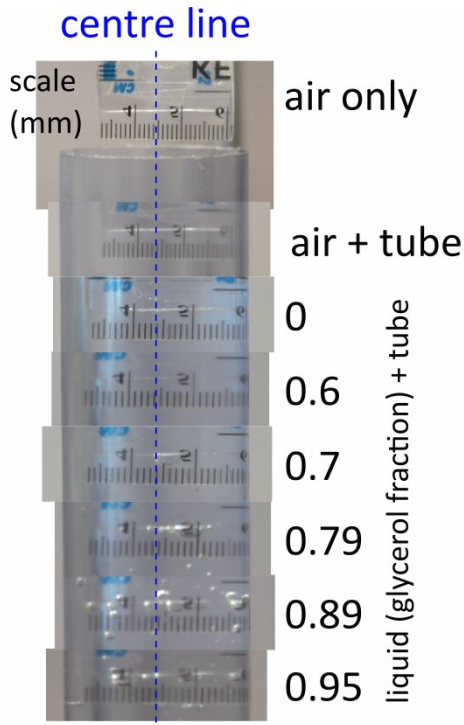
The summation $\sum_{i=1}^n e_i^2$ denotes the sum of the squares of the individual errors.

For this specific calculation, the error values e_1 and e_2 correspond to the distortion error and the precision error, respectively.

Appendix 4. Refraction corrections

4.1. Experimental quantification of distortion

To quantify distortion caused by refraction through the tube wall and liquids along the boundaries of the tube cross-section, we imaged a ruler in air, in the empty tube, and in the tube filled with each liquid Appendix Figure 1. A web plot digitizer was then used to establish a known scale based on the tube radius (centre line to tube edge = 20 mm) then determine the actual and apparent radial distances starting from the centreline towards the edges. We found that pixel scale varies with increasing distance from the centreline of the tube. This has particular implications for measurements taken across the tube diameter i.e., falling film thickness and bubble diameter.



500 **Appendix Figure 1: Illustration of imaging used to quantify distortion along the tube cross-section.**

4.2. Model methods

Optical system and ray tracing

To consider refraction at the tube-glass interface where imaged rays are not orthogonal to the surfaces, we developed a ray-tracing model to calculate optical distortion in cylindrical PVC tubes filled with glycerol-water mixtures using Snell's law.

505 The tube geometry consisted of an inner radius $r_{inner} = 18 \text{ mm}$, and outer radius $r_{outer} = 20 \text{ mm}$, yielding a wall thickness of 2 mm.

For the optical properties, we used the refractive indices of $n_{air} = 1.000$, $n_{water} = 1.333$, $n_{glycerol} = 1.474$ and $n_{pvc} = 1.540$. The refractive index of the glycerol-water mixtures was calculated using a linear mixing rule:

$$n_{fluid} = n_{water}(1 - f_g) + n_{glycerol}f_g \quad (2)$$

510 where f_g represents the glycerol volume fraction.

Calculation of ray paths

For an object at radial position r from the tube centre, we traced rays through the system by calculating the incident angle at the inner surface:

$$\theta_{incident} = \arcsin \frac{r}{r_{inner}} \quad (3)$$

Applying Snell's law at the fluid-PVC interface:

$$\sin\theta_{pvc} = \frac{n_{fluid}}{n_{pvc}} \sin\theta_{incident} \quad (4)$$

Calculating the path length through the tube wall:

$$L = \frac{r_{outer} - r_{inner}}{\cos\theta_{pvc}} \quad (5)$$

520 At the PVC-air interface, we calculated the exit angle:

$$\sin\theta_{air} = \frac{n_{pvc}}{n_{air}} \sin\theta_{pvc} \quad (6)$$

Positions where $\sin\theta_{air} > 1$ indicate total reflection, rendering the object invisible at that location.

Apparent position model

525 To match experimental observations, we developed an empirical demagnification model. Minimal distortion occurs in air-filled tubes:

$$\text{demagnification}_{air} = 1.0 - 0.01 \left(\frac{r}{r_{inner}} \right)^2 \quad (7)$$

For liquid-filled tubes, we implemented a three-component model combining angular compression, index mismatch, and edge effects:

$$\text{demagnification}_{liquid} = \frac{\sin\theta_{pvc}}{\sin\theta_{incident}} \times \frac{n_{fluid}}{n_{pvc}} \times \left[1.0 - 0.2 \left(\frac{r}{r_{inner}} \right) \right]^2 \quad (8)$$

530 The apparent radial position is then:

$$\text{demagnification}_{liquid} = r \times \text{demagnification} \quad (9)$$

Experimental validation

The collected experimental data were loaded with the format "XXpercent.csv" where XX indicates the relevant glycerol percentage.

535 ***Model limitations and extrapolation***

The simplified ray-tracing model predicts total internal reflection (TIR) at the PVC-air interface for radial positions beyond approximately 14 mm, where the calculated exit angle of $\theta_c = \arcsin(1/1.54) \approx 42.2$. However, the experimental data clearly shows that objects remain visible up to 17.88 mm, indicating that the single-ray approximation fails to capture the complete physics.

540 This discrepancy arises because the model considers only a direct ray path from object to observer, where in reality objects emit light in multiple directions. Rays travelling at different angles can successfully traverse the optical system even when the

direct ray undergoes TIR. The visibility of objects near the tube edge is maintained through these alternative ray paths, though with severe optical compression.

To reconcile the theory with the experimental data as closely as possible, we applied a third-degree polynomial extrapolation using the last 30 valid data points to extend the theoretical curves from 14 mm to 18 mm. This approach preserves the model's accuracy in the central region while providing reasonable estimates for the edge behaviour where the single-ray approximation breaks down.

Data Analysis

We compared the theoretical predictions with the experimental measurements by calculating the apparent position for each experimental datapoint and computing the mean absolute percentage error:

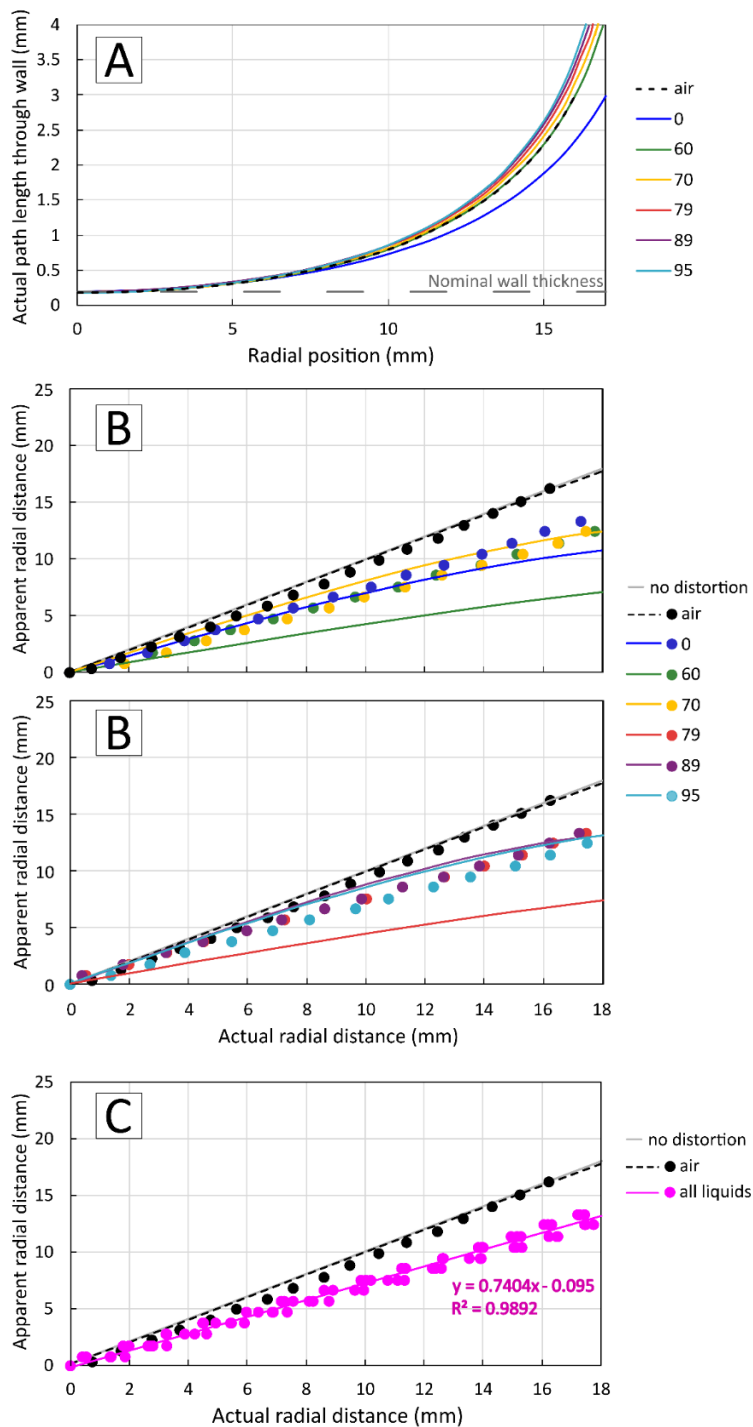
$$Error = \frac{1}{N} \sum_{i=1}^N \left| \frac{r_{apparent,theory} - r_{apparent,exp}}{r_{apparent,exp}} \right| \times 100 \quad (1010)$$

Additionally, we generated visualisations for glycerol concentrations of 0, 60, 70, 79, 89, and 95 % to demonstrate the increasing optical distortion with refractive index.

Appendix Figure 2A shows the calculated ray path lengths through the tube wall, and a comparison of the predicted (Snell's law) and measured (experimental) optical distortion as it occurs with increasing radial distance from the centre point (0). The distortion through the liquids is shown to occur over a small range with a linear fit where $R^2 = 0.99$. As such, we used its line equation to apply the correction to the diameter and falling film thickness data obtained using measurement ROI method (b) described above. The code (written by ECPB) is available for download via the link at the end of the paper.

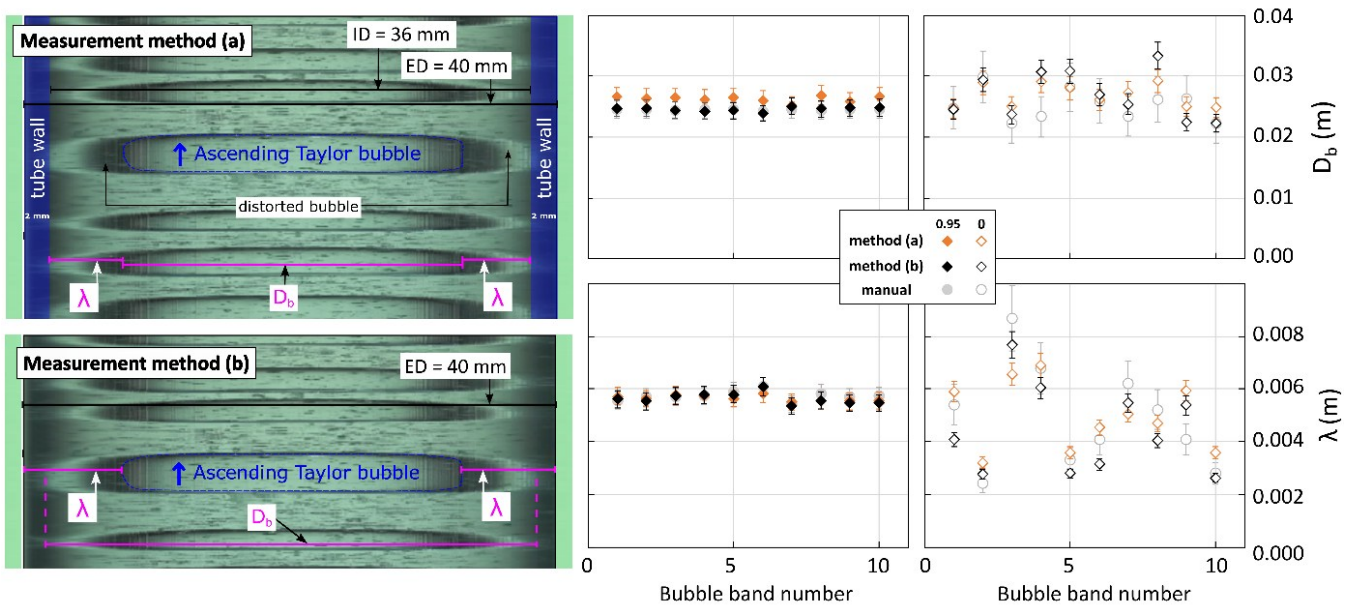
Results

We find that distortion can be accounted for directly on the kymographs by (a) using known measurable boundaries to identify what is and is not 'bubble' or 'falling film' in the kymograph i.e., by drawing the line ROI to cover the minimum bubble boundary and excluding visible distortion, or by (b) including visible regions of distortion during ROI selection then applying a correction to the data retroactively. Both parameters can be accurately measured on the kymograph using these methods (Appendix Figure 3). The data presented in the main text utilises method (a). The correction applied to the data in method (b) utilises the line equation derived from the experimental data demonstrated in Appendix Figure 2 in pink. Refraction-driven distortion corrections for velocity, length etc. kymographs are not needed because the measurement ROIs are drawn along the centreline of the tube parallel to the direction of ascent; distortion along the edges of the FOV are caused by the lens and captured within the calculated error. The accuracy of these methods is evidenced by the good agreement of the kymograph data with theoretical predictions or experimental data from the literature for each relevant parameter.



570

Appendix Figure 2: [A] shows the calculated ray path length through the tube wall, [B] plots show the theoretical (solid lines) vs experimentally quantified (markers) optical distortion (these were split into two separate plots so that overlapping data can be viewed clearly), and [C] shows the experimentally measured optical distortion for all liquid on a single plot, and the line equation used to apply distortion correction to the data as described in the appended text.



575

Appendix Figure 3: Annotated kymograph showing measurement ROI selections based on methods (a) – accounting for refraction during measurement ROI selection – or (b) – correcting for refraction mathematically later – as described in the Appendix text. Since the region of distortion is corrected for in method (b), it must be included in measurement ROI selections for both parameters i.e., the line ROIs overlap. The plots show the agreement between the two methods for both diameter and falling film thickness measurements.

580

Appendix 5. Image filtering / thresholding

Image filtering and thresholding techniques were attempted both during image pre-processing, and to the kymographs themselves, to try to remove or attenuate image noise. These include the Gaussian, median, minimum, maximum, and variance filters that are built into imageJ, and also the Fourier-transform based and ROI-width filtering algorithms that are part of imageJ kymograph plugins (DynamicKymograph: <https://imagej.net/plugins/dynamic-kymograph> and KymographDirect (Mangeol *et al.*, 2016)). All attempts were unsuccessful and limited overall measurement accuracy. Filtering eroded the boundaries representing key bubble and liquid features required for measurement either via a reduction in image sharpness, or by enhancing regions of glare or shadow. Automation of this technique was also unsuccessful for similar reasons. As kymography is further refined, particularly through advances in imaging and AI, its utility in volcanology is likely to expand.

585

590 Appendix 6. Gas volume fraction model

To predict the gas volume fraction (GVF) in an experiment using known pump voltage and liquid viscosity values, we first characterised the behaviour of the pump and its influence on GVF. The GVF peak values (maximum GVF reached for each pump voltage and liquid viscosity) obtained using the kymograph method described in Section 2.7. were compiled into a CSV

file (column AA in the supplied datasheet supplied with the supplementary files). A custom Python script was written by *ECPB* to analyse this dataset and model the relationship between GVF, pump voltage, and fluid viscosity (the code is available in the supplementary material). The script groups the dataset by unique voltage values (minimum of six unique values required to ensure adequate coverage for model fitting) then calculates the mean GVF peak, the standard deviation, the number of samples, and the average viscosity for each voltage group.

A multi-parameter nonlinear model is fitted using differential evolution optimisation to predict GVF peaks as a function of both voltage and viscosity. The functional form of the model is:

$$GVF_{peaks} = a \cdot V^b \cdot \mu^c + d \cdot V + e \quad (11)$$

Where V is the pump voltage, μ is the dynamic viscosity of the fluid, and a , b , c , d , and e are fitted model parameters: a is a scale factor, b indicates the sensitivity of GVF to pump voltage, c indicates the sensitivity of GVF to liquid viscosity, $d \cdot V$ is a linear component, and e is a constant. This model form was selected to search for the best values of a , b , c , d , and e that minimise the difference between the model's predictions and the actual GVF values we determined using the kymograph method.

Model performance was evaluated using R^2 , root mean square error (RMSE), and residual statistics. The final model showed a high degree of explanatory power ($R^2=0.95$), with a typical prediction uncertainty of $\pm 3.2\%$ RMSE. Uncertainty intervals (e.g., 95% confidence = $\pm 2 \times$ RMSE) were also reported to support predictive use in future experiments. A bootstrap resampling procedure was applied to estimate parameter uncertainties; this enabled the calculation of 95% confidence intervals for each model coefficient. The model results are summarised below; model uncertainty bands, residual analysis plots and the distribution of residuals are displayed in Appendix Figure 4.

Model equation:

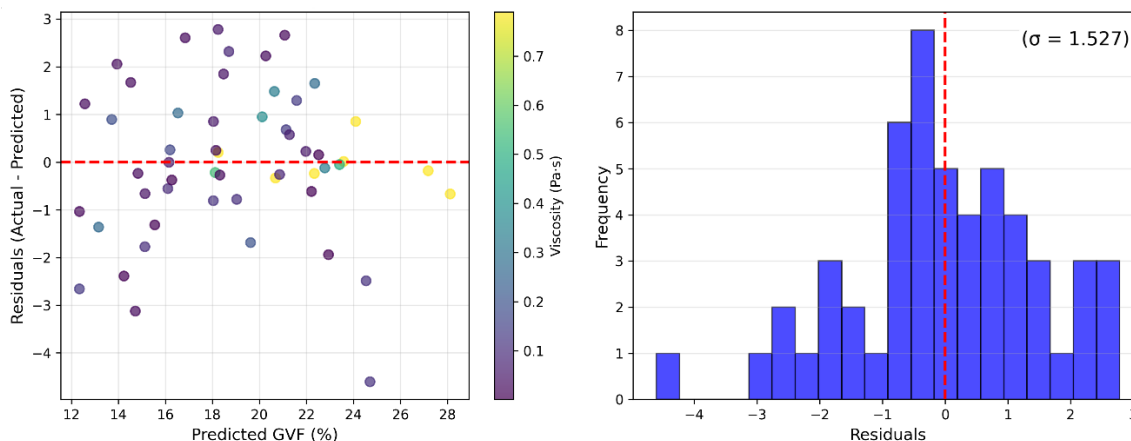
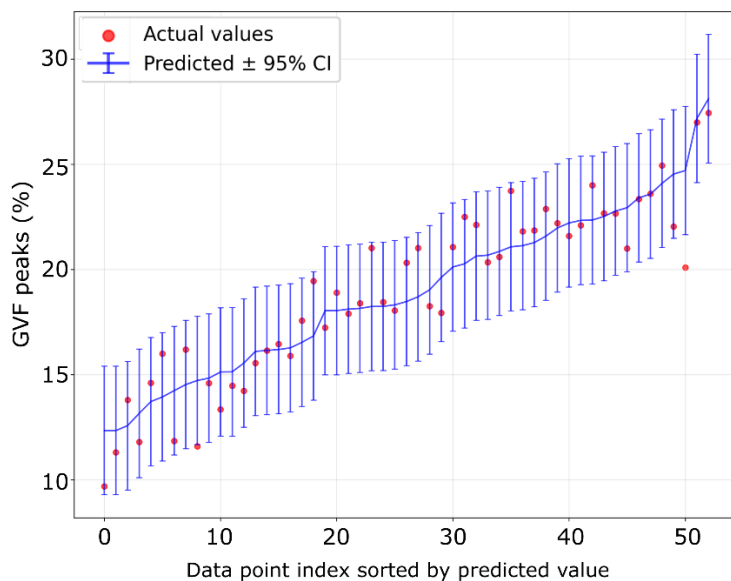
$$GVF_{peaks} = 16.465 \cdot V^{-0.491} \cdot \mu^{1.668} + 2.789 \cdot V + 1.884 \quad (12)$$

With $R^2 = 0.863$, the error to report for GVF peaks predictions is:

- RMSE = 1.53% (root mean square error).
- For individual predictions: $\pm 3.1\%$ at 95% confidence level.
- For average/expected predictions: $\pm 1.5\%$ at $\sim 68\%$ confidence level.

This means that for any given (μ , V) combination, we can expect:

- 68% of predictions to be within $\pm 1.5\%$ of the true value.
- 95% of predictions to be within $\pm 3.1\%$ of the true value.
- 99% of predictions to be within $\pm 3.9\%$ of the true value.



625 **Appendix Figure 4: Plots showing uncertainty analysis at the 95 % confidence interval (top), and residual analysis results with the distribution of residuals (bottom left and right, respectively) from the GVF model described in the appended text.**

Appendix 7. Unedited kymographs

630 The kymographs shown in the main text are small segments of the raw kymographs that have been cut down and annotated for simplicity and clarity. A sample of unedited kymographs are available as .TIFF files in the supplementary material (see “Data, code, video and kymograph availability”) under the following filename classification: “[camera FOV]_[glycerol content]_[pump voltage]” e.g., “close-up_0.95_12V” corresponds to a kymograph generated from close-up FOV footage of bubbles ascending in 0.95 glycerol content where the pump voltage input is set to 12 Volts.

Supplementary files – the data, code, experimental footage and kymographs

Data are available for download in the following data repository: <https://doi.org/10.5281/zenodo.16037059>.

635 Code for the ray tracing model (distortion) described in Appendix 4.2 is available for download in the following repository:
<https://doi.org/10.5281/zenodo.16038113>.

Code for the GVF prediction model described in Appendix 6 is available for download in the following repository:
<https://doi.org/10.5281/zenodo.16109361>.

Raw kymographs are for download in the following repository: <https://doi.org/10.5281/zenodo.16039125>

640 Experimental footage files are available for download in the following repository: <https://doi.org/10.5281/zenodo.16040076>

Author contribution

Hannah Calleja: Conceptualisation, Investigation, Validation, Formal Analysis, Methodology, Data curation, Visualisation, Writing – original draft, Writing – review & editing. **Eric C.P. Breard:** Writing – review & editing, Conceptualisation, Methodology. **Tom D. Pering:** Writing – review & editing, Conceptualisation, Resources. **Linda A. Kirstein:** Writing –
645 review & editing, Funding acquisition. **Ian B. Butler:** Writing – review & editing, Funding acquisition. **J. Godfrey Fitton:**
Writing – review & editing, Funding acquisition.

Declaration of competing interests

The authors declare that they have no conflict of interest.

Declaration of generative AI and AI assisted technologies

650 During the preparation of this work the authors used the ELM – Edinburgh (access to) Language Models – service to improve
the readability of parts of the manuscript, aid in literature searches, and format the reference list. ELM is the University of
Edinburgh's AI innovation platform, a central gateway providing safer access to Generative Artificial Intelligence (GAI) via
access to Large Language Models (LLMs). ELM has a Zero Data Retention policy in place with OpenAI. Use of the service
was applied with careful human oversight, rigorous review, and editing as needed. The authors take full responsibility for the
655 content of the published article.

Acknowledgements

The authors acknowledge Michael Manga whose kymograph work on cluster-induced turbulence and multi-phase flows initially inspired this work. We thank Claudia Elias Parra and Eilidh Vass Payne for their support and insightful comments, which improved the content and presentation of this research. The authors appreciate the comments and suggestions provided by the anonymous reviewers which improved the manuscript.

Financial support

This work was supported by funding from the NERC E4 DTP award NE/S007407/1. ECPB was funded by NERC award NE/V014242/1.

References

- Abdulkadir, M., Zhao, D., Sharaf, S., Abdulkareem, L., Lowndes, I. S., and Azzopardi, B. J.: Interrogating the effect of 90° bends on air-silicone oil flows using advanced instrumentation, *Chem Eng Sci*, 66, 2453–2467, <https://doi.org/10.1016/j.ces.2011.03.006>, 2011.
- Abdulkadir, M., Kajero, O. T., Zhao, D., Al-Sarkhi, A., and Hunt, A.: Experimental investigation of liquid viscosity's effect on the flow behaviour and void fraction in a small diameter bubble column: How much do we know?, *J Pet Sci Eng*, 207, <https://doi.org/10.1016/j.petrol.2021.109182>, 2021a.
- Abdulkadir, M., Ugwoke, B., Abdulkareem, L. A., Zhao, D., and Hernandez-Perez, V.: Experimental investigation of the characteristics of the transition from spherical cap bubble to slug flow in a vertical pipe, *Exp Therm Fluid Sci*, 124, 110349, <https://doi.org/10.1016/J.EXPTHERMFLUSCI.2021.110349>, 2021b.
- Ambrose, S.: *The rise of Taylor bubbles in vertical pipes*, 2015.
- Aql, A. and Al-Safran, E.: Investigation of Taylor bubble behavior in upward and downward vertical and inclined pipe flows, *Geoenergy Science and Engineering*, 242, <https://doi.org/10.1016/j.geoen.2024.213194>, 2024.
- Bürkle, F., Maestri, R., Lecrivain, G., et al.: Investigation of the gas and film flow of Taylor bubble in a tube with a short constriction employing 3D particle tracking, *Exp Comput Multiph Flow*, 7, 167–177, <https://doi.org/10.1007/s42757-024-0213-2>, 2025.

- de Azevedo, M. B., Santos, D. dos, Faccini, J. L. H., and Su, J.: Experimental study of the falling film of liquid around a Taylor bubble, *International Journal of Multiphase Flow*, 88, 133–141, <https://doi.org/10.1016/j.ijmultiphaseflow.2016.09.021>, 2017.
- 690 Del Bello, E., Llewellyn, E. W., Taddeucci, J., Scarlato, P., and Lane, S. J.: An analytical model for gas overpressure in slug-driven explosions: Insights into Strombolian volcanic eruptions, *J Geophys Res Solid Earth*, 117, <https://doi.org/10.1029/2011JB008747>, 2012.
- 695 Del Bello, E., Lane, S. J., James, M. R., Llewellyn, E. W., Taddeucci, J., Scarlato, P., and Capponi, A.: Viscous plugging can enhance and modulate explosivity of strombolian eruptions, *Earth Planet. Sci. Lett.*, 423, 210–218, <https://doi.org/10.1016/j.epsl.2015.04.034>, 2015.
- 700 Benattalah, S., Aloui, F., and Souhar, M.: Experimental analysis on the counter-current Dumitrescu-Taylor bubble flow in a smooth vertical conduct of small diameter, *Journal of Applied Fluid Mechanics*, 4, 1–14, <https://doi.org/10.36884/jafm.4.04.11940>, 2011.
- De Bertodano, M. L., Sun, X., Ishii, M., and Ulke, A.: Phase Distribution in the Cap Bubble Regime in a Duct, *J Fluids Eng*, 128, 811–818, <https://doi.org/10.1115/1.2201626>, 2006.
- 705 Browne, C. A., Shih, A., and Datta, S. S.: Pore-Scale Flow Characterization of Polymer Solutions in Microfluidic Porous Media, <https://doi.org/10.1002/sml.201903944>, 2020.
- Bugg, J. D. and Saad, G. A.: The velocity field around a Taylor bubble rising in a stagnant viscous fluid: Numerical and experimental results, *International Journal of Multiphase Flow*, 28, 791–803, [https://doi.org/10.1016/S0301-9322\(02\)00002-2](https://doi.org/10.1016/S0301-9322(02)00002-2), 2002.
- 710 Calleja, H. and Pering, T.: Crystals and inclined conduits: analogue experiments for slug-driven volcanism, *Volcanica*, 6, 147–160, <https://doi.org/10.30909/vol.06.01.147160>, 2023.
- 715 Calleja, H., Breard, E.C.P., Pering, T.D., Kirstein, L.A., Butler, B.I., Fitton, J.G.: Dataset for Calleja et al. “Experimental analysis of Taylor bubble regimes using kymography”., Zenodo, <https://doi.org/10.5281/zenodo.16037059>, 2025a.
- 720 Calleja, H., Breard, E.C.P., Pering, T.D., Kirstein, L.A., Butler, B.I., Fitton, J.G.: distortion_code [for Calleja et al. “Experimental analysis of Taylor bubble regimes using kymography”], Zenodo, <https://doi.org/https://doi.org/10.5281/zenodo.16038113>, 2025b.

- Calleja, H., Breard, E.C.P., Pering, T.D., Kirstein, L.A., Butler, B.I., Fitton, J.G.: GVF-prediction_code [for Calleja et al. “Experimental analysis of Taylor bubble regimes using kymography”], Zenodo, <https://doi.org/https://doi.org/10.5281/zenodo.16109361>, 2025c.
- 725 Calleja, H., Breard, E.C.P., Pering, T.D., Kirstein, L.A., Butler, B.I., Fitton, J.G.: Sample experiment footage [for Calleja et al. “Experimental analysis of Taylor bubble regimes using kymography”], Zenodo, <https://doi.org/10.5281/zenodo.16040076>, 2025d.
- Calleja, H., Breard, E.C.P., Pering, T.D., Kirstein, L.A., Butler, B.I., Fitton, J.G. : Unedited kymographs [for Calleja et al. “Experimental analysis of Taylor bubble regimes using kymography”], Zenodo, <https://doi.org/10.5281/zenodo.16039125>, 2025e.
- 730
- Campos, J. B. L. M. and Guedes De Carvalho, J. R. F.: An experimental study of the wake of gas slugs rising in liquids, *J Fluid Mech*, 196, 27–37, <https://doi.org/10.1017/S0022112088002599>, 1988.
- 735
- Capponi, A., James, M. R., and Lane, S. J.: Gas slug ascent in a stratified magma: Implications of flow organisation and instability for Strombolian eruption dynamics, *Earth Planet Sci Lett*, 435, 159–170, <https://doi.org/10.1016/j.epsl.2015.12.028>, 2016.
- 740
- Cerqueira, R. F. L. and Paladino, E. E.: Experimental study of the flow structure around Taylor bubbles in the presence of dispersed bubbles, *International Journal of Multiphase Flow*, 133, <https://doi.org/10.1016/j.ijmultiphaseflow.2020.103450>, 2020.
- 745
- Davies, R. M. and Taylor, G.: The mechanics of large bubbles rising through extended liquids and through liquids in tubes, *Proc R Soc Lond A Math Phys Sci*, 200, 375–390, <https://doi.org/10.1098/RSPA.1950.0023>, 1950.
- Eibl, E. P. S., Thordarson, T., Höskuldsson, Á., Gudnason, E., Dietrich, T., Hersir, G. P., and Ágústsdóttir, T.: Evolving shallow conduit revealed by tremor and vent activity observations during episodic lava fountaining of the 2021 Geldingadalir eruption, Iceland, *Bull Volcanol*, 85, <https://doi.org/10.1007/s00445-022-01622-z>, 2023.
- 750
- Etminan, A., Muzychka, Y. S., and Pope, K.: A review on the hydrodynamics of Taylor flow in microchannels: Experimental and computational studies, <https://doi.org/10.3390/pr9050870>, 2021.

- 755 Gardner, J. E., Wadsworth, F. B., Carley, T. L., Llewellyn, E. W., Kusumaatmaja, H., and Sahagian, D.: Bubble Formation in Magma, 51, <https://doi.org/10.1146/annurev-earth-031621-080308>, 2022.
- Gaudin, D.: Integrating puffing and explosions in a general scheme for Strombolian-style activity, *J. Geophys. Res. Solid Earth.*, 122, 1860–1875, <https://doi.org/10.1002/2016JB013707>, 2017.
- 760 Gaudin, D., Taddeucci, J., Scarlato, P., del Bello, E., Ricci, T., Orr, T., Houghton, B., Harris, A., Rao, S., and Bucci, A.: Integrating puffing and explosions in a general scheme for Strombolian-style activity, *J Geophys Res Solid Earth*, 122, 1860–1875, <https://doi.org/10.1002/2016JB013707>, 2017.
- Haward, S. J., Hopkins, C. C., and Shen, A. Q.: Stagnation points control chaotic fluctuations in viscoelastic porous media
765 flow, <https://doi.org/10.1073/pnas.2111651118/-/DCSupplemental.y>, 2021.
- James, M. R., Lane, S. J., Chouet, B., and Gilbert, J. S.: Pressure changes associated with the ascent and bursting of gas slugs in liquid-filled vertical and inclined conduits, *Journal of Volcanology and Geothermal Research*, 129, 61–82, [https://doi.org/10.1016/S0377-0273\(03\)00232-4](https://doi.org/10.1016/S0377-0273(03)00232-4), 2004.
770
- James, M. R., Lane, S. J., and Chouet, B. A.: Gas slug ascent through changes in conduit diameter: Laboratory insights into a volcano-seismic source process in low-viscosity magmas, *J Geophys Res Solid Earth*, 111, <https://doi.org/10.1029/2005JB003718>, 2006.
- 775 James, M. R., Lane, S. J., and Corder, S. B.: Modelling the rapid near-surface expansion of gas slugs in low-viscosity magmas, *Geological Society, London, Special Publications*, 307, 147–167, <https://doi.org/10.1144/SP307.9>, 2008.
- James, M. R., Lane, S. J., Wilson, L., and Corder, S. B.: Degassing at low magma-viscosity volcanoes: Quantifying the transition between passive bubble-burst and Strombolian eruption, *Journal of Volcanology and Geothermal Research*, 180,
780 81–88, <https://doi.org/10.1016/J.JVOLGEORES.2008.09.002>, 2009.
- Jaupart, C. and Vergnolle, S.: Laboratory models of Hawaiian and Strombolian eruptions, *Nature*, 331, 58–60, <https://doi.org/10.1038/331058a0>, 1988.
- 785 Jaupart, C. and Vergnolle, S.: The Generation and Collapse of a foam Layer at the Roof of a Basaltic Magma Chamber, *J Fluid Mech*, 203, 347–380, <https://doi.org/10.1017/S0022112089001497>, 1989.

Kang, C. W., Quan, S., and Lou, J.: Numerical study of a Taylor bubble rising in stagnant liquids, *Phys Rev E Stat Nonlin Soft Matter Phys*, 81, <https://doi.org/10.1103/PhysRevE.81.066308>, 2010.

790

Karapantsios, T. D. and Karabelast, A. J.: Longitudinal characteristics of wavy falling films, *Int. J. Multiphase Flow*, 119–127, [https://doi.org/10.1016/0301-9322\(94\)00048-O](https://doi.org/10.1016/0301-9322(94)00048-O), 1995.

Kawaji, M., Dejesus, J. M., and Tudose, G.: Investigation of flow structures in vertical slug flow, *Nuclear Engineering and Design*, 175, 37–48, [https://doi.org/10.1016/S0029-5493\(97\)00160-X](https://doi.org/10.1016/S0029-5493(97)00160-X), 1997.

795

Kemper, P., Küstermann, E., Dreher, W., Helmers, T., Mießner, U., Besser, B., and Thöming, J.: Magnetic Resonance Imaging for Non-invasive Study of Hydrodynamics Inside Gas-Liquid Taylor Flows, *Chem Eng Technol*, 44, 465–476, <https://doi.org/10.1002/ceat.202000509>, 2021.

800

Kobayashi, T., Namiki, A., and Sumita, I.: Excitation of airwaves caused by bubble bursting in a cylindrical conduit: Experiments and a model, *J Geophys Res Solid Earth*, 115, <https://doi.org/10.1029/2009JB006828>, 2010.

Lane, S. J., James, M. R., and Corder, S. B.: Volcano infrasonic signals and magma degassing: First-order experimental insights and application to Stromboli, *Earth Planet Sci Lett*, 377–378, 169–179, <https://doi.org/10.1016/j.epsl.2013.06.048>, 2013.

805

Le, A. V. and Fenech, M.: Image-Based Experimental Measurement Techniques to Characterize Velocity Fields in Blood Microflows, <https://doi.org/10.3389/fphys.2022.886675>, 2022.

Lehr, J., and Rabbel, W.: Magnitude and Interevent Time Statistics of Strombolian Activity of Villarrica Volcano and Inference Regarding the Flow Regime, *J Geophys Res Solid Earth*, 126, <https://doi.org/10.1029/2021JB021658>, 2021.

810

Lel, V. V., Al-Sibai, F., Leefken, A., and Renz, U.: Local thickness and wave velocity measurement of wavy films with a chromatic confocal imaging method and a fluorescence intensity technique, *Exp Fluids*, 39, 856–864, <https://doi.org/10.1007/s00348-005-0020-x>, 2005.

815

Llewellyn, E. W., Del Bello, E., Taddeucci, J., Scarlato, P., and Lane, S. J.: The thickness of the falling film of liquid around a Taylor bubble, *Proceedings of the Royal Society A: Mathematical, Physical and Engineering Sciences*, 468, 1041–1064, <https://doi.org/10.1098/RSPA.2011.0476>, 2012.

820

- Mangeol, P., Prevo, B., and Peterman, E. J. G.: KymographClear and KymographDirect: Two tools for the automated quantitative analysis of molecular and cellular dynamics using kymographs, *Mol Biol Cell*, 27, 1948–1957, <https://doi.org/10.1091/mbc.E15-06-0404>, 2016.
- 825 Manta, F., Emadzadeh, A., and Taisne, B.: New Insight Into a Volcanic System: Analogue Investigation of Bubble-Driven Deformation in an Elastic Conduit, *J Geophys Res Solid Earth*, 124, 11274–11289, <https://doi.org/10.1029/2019JB017665>, 2019.
- Marié, J.-L.: Investigation of two-phase bubbly flows using laser doppler anemometry, *physico-Chemical Hydrodynamics*, 830 4(2), 103-118, 1983.
- Maruishi, T. and Toramaru, A.: Rapid Coalescence of Bubbles Driven by Buoyancy Force: Implication for Slug Formation in Basaltic Eruptions, *J Geophys Res Solid Earth*, 129, <https://doi.org/10.1029/2024JB029130>, 2024.
- 835 Metzker, L. F., Araújo, C. C. S., Figueiredo, M. M. F., and Fileti, A. M. F.: Computer vision techniques for Taylor bubble detection and velocity measurement using YOLO v8 and optical flow, *Flow Meas Instrum*, 104, 102885, <https://doi.org/10.1016/j.flowmeasinst.2025.102885>, 2025
- Morgado, A. O., Miranda, J. M., Araújo, J. D. P., and Campos, J. B. L. M.: Review on vertical gas–liquid slug flow, 840 *International Journal of Multiphase Flow*, 85, 348–368, <https://doi.org/10.1016/J.IJMULTIPHASEFLOW.2016.07.002>, 2016.
- Muñoz, V., Walter, T. R., Zorn, E. U., Shevchenko, A. V., González, P. J., Reale, D., and Sansosti, E.: Satellite Radar and Camera Time Series Reveal Transition from Aligned to Distributed Crater Arrangement during the 2021 Eruption of Cumbre Vieja, La Palma (Spain), *Remote Sens (Basel)*, 14, <https://doi.org/10.3390/rs14236168>, 2022.
- 845 Nogueira, S., Sousa, R. G., Pinto, A. M. F. R., Riethmuller, M. L., and Campos, J. B. L. M.: Simultaneous PIV and pulsed shadow technique in slug flow: A solution for optical problems, *Exp Fluids*, 35, 598–609, <https://doi.org/10.1007/s00348-003-0708-8>, 2003.
- 850 Nogueira, S., Riethmuller, M. L., Campos, J. B. L. M., and Pinto, A. M. F. R.: Flow in the nose region and annular film around a Taylor bubble rising through vertical columns of stagnant and flowing Newtonian liquids, *Chem Eng Sci*, 61, 845–857, <https://doi.org/10.1016/j.ces.2005.07.038>, 2006.

- 855 Nusselt, W.: The Condensation of Steam on Cooled Surfaces., *Zeitschrift Des Vereines Deutscher Ingenieure*, 60, 541–575, 1916.
- Pak, T., Archilha, N. L., Mantovani, I. F., Moreira, A. C., and Butler, I. B.: The Dynamics of Nanoparticle-enhanced Fluid Displacement in Porous Media - A Pore-scale Study, *Sci Rep*, 8, <https://doi.org/10.1038/s41598-018-29569-2>, 2018.
- 860 Parfitt, E. A.: A discussion of the mechanisms of explosive basaltic eruptions, *Journal of Volcanology and Geothermal Research*, 134, 77–107, <https://doi.org/10.1016/J.JVOLGEORES.2004.01.002>, 2004.
- Parfitt, E. A. and Wilson, L.: Explosive volcanic eruptions—IX. The transition between Hawaiian-style lava fountaining and Strombolian explosive activity, *Geophys J Int*, 121, 226–232, <https://doi.org/10.1111/J.1365-246X.1995.TB03523.X>, 1995.
- 865 Penlou, B., Roche, O., Manga, M., and van den Wildenberg, S.: Experimental Measurement of Enhanced and Hindered Particle Settling in Turbulent Gas-Particle Suspensions, and Geophysical Implications, *J Geophys Res Solid Earth*, 128, <https://doi.org/10.1029/2022JB025809>, 2023.
- 870 Pering, T. D. and McGonigle, A. J. S.: Combining Spherical-Cap and Taylor Bubble Fluid Dynamics with Plume Measurements to Characterize Basaltic Degassing, *Geosciences* 2018, Vol. 8, Page 42, 8, 42, <https://doi.org/10.3390/GEOSCIENCES8020042>, 2018.
- 875 Pering, T. D., McGonigle, A. J. S., James, M. R., Tamburello, G., Aiuppa, A., Delle Donne, D., and Ripepe, M.: Conduit dynamics and post explosion degassing on Stromboli: A combined UV camera and numerical modeling treatment, *Geophys Res Lett*, 43, 5009–5016, <https://doi.org/10.1002/2016GL069001>, 2016.
- 880 Roitberg, E., Barnea, D., and Shemer, L.: International Journal of Multiphase Flow Elongated bubble shape in inclined air-water slug flow, *International Journal of Multiphase Flow*, 85, 76–85, <https://doi.org/10.1016/j.ijmultiphaseflow.2016.05.011>, 2016.
- Schneider, C. A., Rasband, W. S., and Eliceiri, K. W.: NIH Image to ImageJ: 25 years of image analysis, <https://doi.org/10.1038/nmeth.2089>, 2012.
- 885 Seyfried, R. and Freundt, A.: Experiments on conduit flow and eruption behavior of basaltic volcanic eruptions, *J Geophys Res Solid Earth*, 105, 23727–23740, <https://doi.org/10.1029/2000JB900096>, 2000.

Shosho, C. E. and Ryan, M. E.: An experimental study of the motion of long bubbles in inclined tubes, *Chemical Engineering Science*, 2191–2204, [https://doi.org/10.1016/S0009-2509\(00\)00504-2](https://doi.org/10.1016/S0009-2509(00)00504-2), 2001.

890

Sparks, R. S. J.: The dynamic of bubble formation and growth in magmas: a review and analysis., *Journal of Volcanology and Geothermal Research*, 1–37, [https://doi.org/10.1016/0377-0273\(78\)90002-1](https://doi.org/10.1016/0377-0273(78)90002-1), 1978.

Spina, L., Taddeucci, J., Pennacchia, F., Morgavi, D., Peña Fernández, J. J., Sesterhenn, J., La Spina, G., and Scarlato, P.: The
895 Effect of Conduit Walls Roughness on Volcanic Jets and Their Seismo-Acoustic Radiation: An Experimental Investigation, *Geophys Res Lett*, 50, <https://doi.org/10.1029/2023GL104717>, 2023.

Suckale, J., Hager, B. H., Elkins-Tanton, L. T., and Nave, J. C.: It takes three to tango: 2. Bubble dynamics in basaltic volcanoes
and ramifications for modeling normal Strombolian activity, *J Geophys Res Solid Earth*, 115, 7410,
900 <https://doi.org/10.1029/2009JB006917>, 2010.

Taddeucci, J., Scarlato, P., Andronico, D., Ricci, T., Civico, R., Del Bello, E., Spina, L., D’Auria, L., Asensio-Ramos, M.,
Calvo, D., Padrón, E., Hernández, P. A., and Pérez, N. M.: The Explosive Activity of the 2021 Tajogaite Eruption (La Palma,
Canary Islands, Spain), *Geochemistry, Geophysics, Geosystems*, 24, <https://doi.org/10.1029/2023GC010946>, 2023.

905

Taitel, Y., Bornea, D., and Dukler, A. E.: Modelling flow pattern transitions for steady upward gas-liquid flow in vertical
tubes, *AIChE Journal*, 26, 345–354, <https://doi.org/10.1002/aic.690260304>, 1980.

Trolese, M., Cerminara, M., Giordano, G., Brand, B. D., Pollock, N., Cifelli, F., and Mattei, M.: Thermal transient PDC
910 behavior induced by topographic drops: A test case at Mt. St. Helens, USA, *Earth Planet Sci Lett*, 627,
<https://doi.org/10.1016/j.epsl.2023.118441>, 2024.

Uhle, D. H., Lube, G., Breard, E. C. P., Meiburg, E., Dufek, J., Ardo, J., Jones, J. R., Brosch, E., Corna, L. R. P., and Jenkins,
S. F.: Turbulent particle-gas feedback exacerbates the hazard impacts of pyroclastic density currents, *Commun Earth Environ*,
915 5, <https://doi.org/10.1038/s43247-024-01305-x>, 2024.

Viana, F., Pardo, R., Yáñez, R., Trallero, J. L., and Joseph, D. D.: Universal correlation for the rise velocity of long gas bubbles
in round pipes, *J Fluid Mech*, 494, 379–398, <https://doi.org/10.1017/S0022112003006165>, 2003.

- 920 Vossen, C. E. J., Cimorelli, C., D'Auria, L., Cigala, V., Kueppers, U., Barrancos, J., and Bennett, A. J.: Explosive eruption style modulates volcanic electrification signals, *Commun Earth Environ*, 5, <https://doi.org/10.1038/s43247-024-01520-6>, 2024.
- Walter, T. R., Belousov, A., Belousova, M., Kotenko, T., and Auer, A.: The 2019 eruption dynamics and morphology at Ebeko
925 volcano monitored by unoccupied aircraft systems (UAS) and field stations, *Remote Sens (Basel)*, 12, <https://doi.org/10.3390/rs12121961>, 2020.
- Walter, T. R., Zorn, E. U., González, P. J., Sansosti, E., Muñoz, V., Shevchenko, A. V., Plank, S. M., Reale, D., and Richter, N.: Late complex tensile fracturing interacts with topography at Cumbre Vieja, La Palma, *Volcanica*, 6, 1–17,
930 <https://doi.org/10.30909/vol.06.01.0117>, 2023.
- Wang, G., Zhang, M., and Ishii, M.: Flow structure of bubbly to slug transition flow in a small pipe, *Int J Heat Mass Transf*, 147, 118943, <https://doi.org/10.1016/J.IJHEATMASSTRANSFER.2019.118943>, 2020.
- 935 Zhang, Z.: A Flexible New Technique for Camera Calibration, Microsoft Research Corporation, Technical Report MSR-TR-98-71 <https://doi.org/https://doi.org/10.1109/34.888718>, 2008.